nature physics

Article

https://doi.org/10.1038/s41567-025-02980-z

The actin cortex acts as a mechanical memory of morphology in confined migrating cells

Received: 8 August 2024

Accepted: 25 June 2025

Published online: 25 August 2025

Check for updates

Yohalie Kalukula[1], Marine Luciano[1], Gleb Simanov[2,3,4], Guillaume Charras[2,3,4], David B. Brückner[5,6,7] ✉ & Sylvain Gabriele[1] ✉

Cell migration in narrow microenvironments occurs in numerous physiological processes. It involves successive cycles of confinement and release that drive important morphological changes. However, it remains unclear whether migrating cells can retain a memory of their past morphological states that could potentially facilitate their navigation through confined spaces. We demonstrate that local geometry governs a switch between two cell morphologies, thereby facilitating cell passage through long and narrow gaps. We combined cell migration assays on standardized microsystems with biophysical modelling and biochemical perturbations to show that migrating cells have a long-term memory of past confinement events. The morphological cell states correlate across transitions through actin cortex remodelling. These findings indicate that mechanical memory in migrating cells plays an active role in their migratory potential in confined environments.

Adherent cells actively adapt their shape and functions to the physicochemical constraints imposed by their surrounding extracellular matrix (ECM) in response to variations in ECM properties[1]. A crucial facet of this adaptive response is the concept of mechanical memory, wherein a new phenotype persists even when the physical constraints are relaxed. Emerging evidence indicates that adherent cells can retain a memory of the mechanical characteristics of their microenvironment after prolonged exposure, ranging from a few days to several weeks, through alterations in transcription factor activity, post-translational modifications and epigenetic changes[2]. Despite these observations, the mechanical memory related to short-duration confinement events that occur repetitively and frequently over hour-long periods during confined migration remains unexplored. In physiologically relevant contexts, cells must interact dynamically with their surroundings to migrate and facilitate processes such as embryogenesis, immune response[3], wound healing[4] and cancer metastasis[5]. Migrating cells must, therefore, adapt their strategies to navigate through mechanically heterogeneous matrices and narrow constrictions, leading to variable confining and unconfining events associated with substantial morphological switches. As adaptation to confinement is potentially energetically costly due to the necessity for transcription and translation, retaining a long-term memory of past confinement may provide a crucial advantage for migrating cells.

A morphological switch is associated with efficient passage through long narrow gaps

To study changes in cell shape during confined migration under standardized and reproducible conditions, we employed a well-established system of adhesive micropatterns featuring a dumbbell geometry, as introduced previously[6–9]. This system consists of a narrow fibronectin (FN) passage, 6 µm in width with a variable length systematically increased from an initial 40 µm up to 80 µm, 120 µm, 160 µm and

[1]SYMBIOSE Lab, Research Institute for Biosciences, CIRMAP, University of Mons – UMONS, Mons, Belgium. [2]London Centre for Nanotechnology, University College London, London, UK. [3]Institute for the Physics of Living Systems, University College London, London, UK. [4]Department of Cell and Developmental Biology, University College London, London, UK. [5]Biozentrum, University of Basel, Basel, Switzerland. [6]Department of Physics, University of Basel, Basel, Switzerland. [7]Institute for Science and Technology Austria, Klosterneuburg, Austria. ✉e-mail: d.b.brueckner@unibas.ch; sylvain.gabriele@umons.ac.be

https://doi.org/10.1038/s41567-025-02980-z

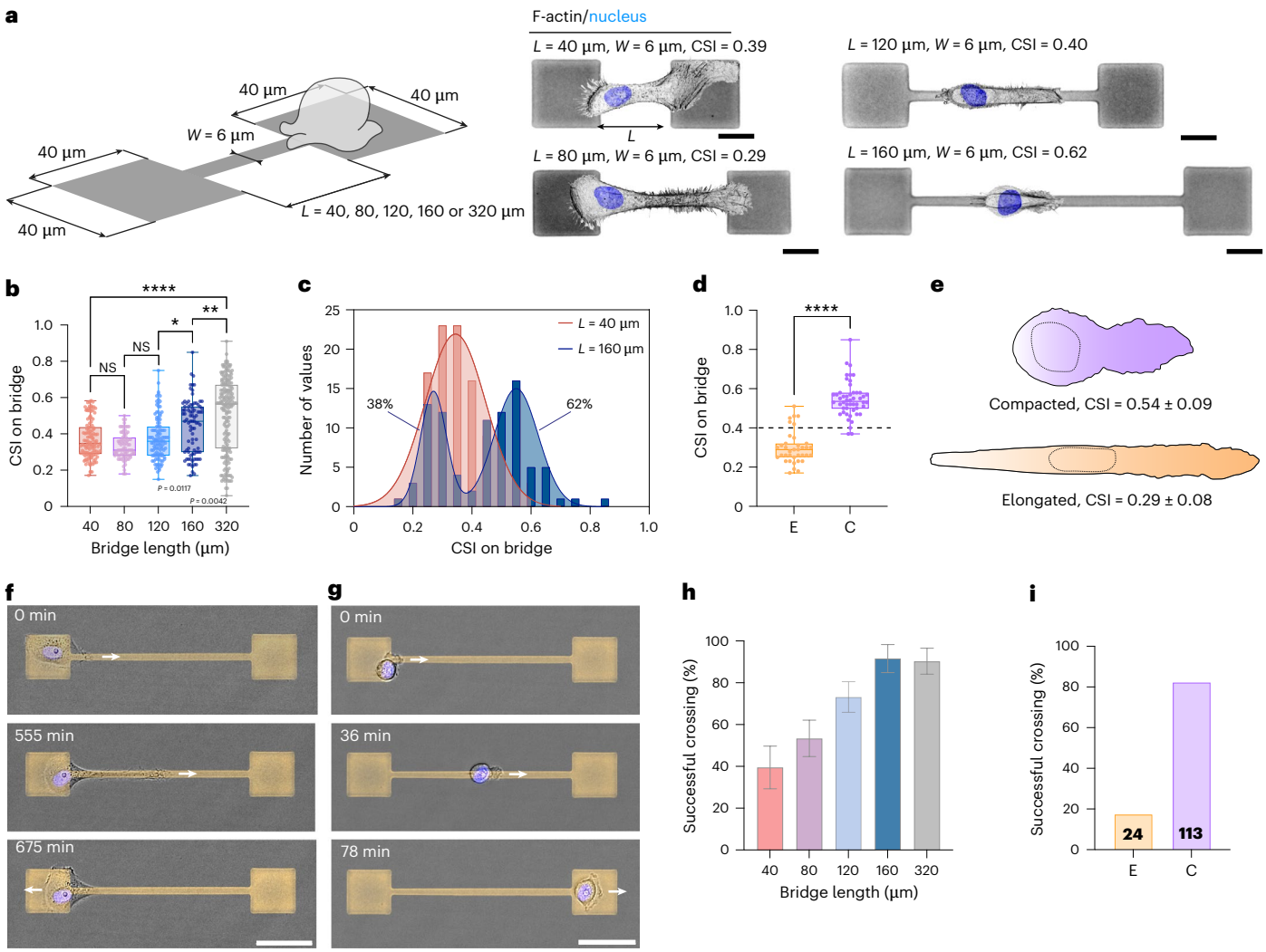

Fig. 1 | A morphological switch ensures a successful crossing on long bridges. **a**, Schematic representation and typical microscopy images of single epithelial cells (MCF-10A) navigating through a narrow passage represented by a dumbbell micropattern. The FN-coated micropattern consists of two square islands of 40 µm × 40 µm connected to a narrow bridge of a constant width (W = 6 µm) and various lengths (L = 40 µm, 80 µm, 120 µm, 160 µm or 320 µm). The nucleus is stained with Hoechst, and actin filaments are stained with phalloidin (colours inverted). The CSI is indicated for each bridge length. **b**, CSI on bridge versus bridge length (n = 116 for 40 µm, n = 76 for 80 µm, n = 109 for 120 µm, n = 87 for 160 µm and n = 184 for 320 µm from $N \geq 3$). *P = 0.0117; **P = 0.0042; ****$P < 0.0001$. **c**, Distribution of the CSI values on the bridge for L = 40 µm (red) and L = 160 µm (blue). **d**, CSI on the bridge for elongated (E, n = 37) and compacted (C, n = 50) epithelial cell morphologies for L = 160 µm. **e**, Schematic representation of the typical morphology of a compacted (CSI = 0.54 ± 0.09) and an elongated (CSI = 0.29 ± 0.08) morphology. **f**,**g**, Time-lapse sequence of a failed (**f**) and a successful (**g**) crossing of a bridge with W = 6 µm and L = 160 µm. Arrows show the direction of migration. **h**,**i**, Percentage of successful crossings for bridges of various lengths (n = 116 for 40 µm, n = 76 for 80 µm, n = 109 for 120 µm, n = 87 for 160 µm and n = 184 for 320 µm from $N \geq 3$ replicates per condition) (**h**) and for elongated (n = 24) versus compacted (n = 113) morphologies for L = 160 µm (**i**). Error bars in **h** represent the s.d. *$P < 0.05$; **$P < 0.01$; ****$P < 0.0001$ (Student's t-test, two-tailed, unequal variances). Box plots range from the first quartile to the third quartile, with the median (50th percentile) indicated by a line. Whiskers extend from the box to the minimum and maximum data points within 1.5 times the interquartile range. Scale bars, 20 µm (**a**), 50 µm (**f**,**g**). NS, not significant.

320 µm (Fig. 1a). These dimensions correspond to those of interstitial spaces found, for instance, in skin[10] and breast tissues[11], which are less than 10 µm in diameter and can extend over 150 µm in length[12]. Each end of the narrow bridge is connected to a large square area (40 × 40 µm^2), which allows the cell to spread and repolarize before traversing the confined passage again (Supplementary Video 1). Interestingly, it has been demonstrated that one-dimensional microstripes, like those used for the bridge, can effectively replicate many characteristics of the rapid, uniaxial migration phenotype observed in fibrillar three-dimensional cell-derived matrices[13]. Quantifying the cell shape index (CSI; Methods)[14] of mammary epithelial cells (MCF-10A) within these confined bridges (Fig. 1b) based on automatic tracking of 20-h-long time-lapse experiments (Supplementary Video 2) revealed a surprising bimodal distribution for the longest length (160 µm; Fig. 1c). This indicates the presence of two distinct subpopulations of cell morphologies with a CSI either below or above 0.4 (Fig. 1d and Supplementary Video 3), corresponding to elongated (~38%) or compacted (~62%) morphologies, respectively (Fig. 1e). As shown in Supplementary Fig. 1, bridges of length 120 µm yielded a unimodal Gaussian CSI distribution (CSI = 0.34 ± 0.09 and R^2 = 0.8257), whereas bridges of length 160 or 320 µm consistently exhibited bimodal distributions. For these longer bridges, the subpopulation means remained notably consistent: 0.27 ± 0.04 and 0.55 ± 0.08 for 160 µm (R^2 = 0.8445) and 0.27 ± 0.08 and 0.55 ± 0.10 for 320 µm (R^2 = 0.9492). These distinct CSI subpopulations indicate the coexistence of different migratory phenotypes, which may reflect underlying differences in cell contractility. Amoeboid phenotypes are typically associated with strong rear-localized phosphorylated myosin light chain (pMLC)

staining, whereas mesenchymal states exhibit a more homogeneous pMLC distribution. To investigate whether these morphological differences reflect pre-existing variations in cellular contractility, we performed immunostaining for pMLC, a key regulator of contractility and actin–myosin cytoskeletal dynamics (Supplementary Fig. 2a). To evaluate the intrinsic contractile state of the initial unconfined cell population, we cultured MCF-10A cells on glass surfaces functionalized with the same concentration of FN used for the micropatterns. Immunostaining revealed a unimodal distribution of pMLC fluorescence intensity (Supplementary Fig. 2b), indicating a continuum of contractility levels rather than discrete subpopulations. These results indicate that the initial MCF-10A population does not exhibit inherent heterogeneity in contractility.

Furthermore, not all crossings were successful, and success seemed to be correlated with CSI. To quantify this observation, we tracked back-and-forth motions by time-lapse imaging for the different bridge lengths. This enabled quantification of the percentage of failed passages (Fig. 1f and Supplementary Video 4), during which cells reversed direction before reaching the square at the opposite end, versus successful passages (Fig. 1g and Supplementary Video 4), during which cells successfully traversed the entire bridge before spreading in the opposite square. Interestingly, we observed that cells crossed longer bridges more efficiently: the probability of an attempt (defined as a protrusion entering the bridge) resulting in a successful transition increased with bridge length, reaching ~91.6% on the longest bridges of 160 µm. Surprisingly, this high rate of successful crossings is directly linked to the compacted morphology (Fig. 1h), which seems to be much more effective in navigating through long and narrow environments (Fig. 1i).

Together, these findings reveal that the emergence of two discrete morphological states—elongated and compacted—occurs only beyond a critical bridge length of 120 µm, which notably exceeds the average maximum elongation capacity of MCF-10A cells (~100 µm). This morphological switch probably reflects an adaptive response to persistent confinement and is associated with efficient migration through long, narrow gaps.

Symmetry-breaking and polarization drive cell-shape dynamics

To explore the link between cell morphology and confined migration efficiency—measured by the percentage of successful crossings—we quantified back-and-forth cell movements over a 20-h period and colour-coded the trajectories based on CSI (Fig. 1d,e), which revealed striking differences in migration dynamics between the two morphologies (Fig. 2a). Compacted cells exhibited an average crossing speed three times faster than elongated morphologies (Fig. 2b) and three times shorter dwell times—defined as the time spent on the square areas—compared with elongated cells (Fig. 2c). An actin flow analysis in the lamellipodia (Fig. 2d and Supplementary Video 5) of both morphologies revealed a significantly higher retrograde flow in compacted cells (Fig. 2e,f), a hallmark of fast-migrating cells[15]. Interestingly, morphological switches from an elongated to a more compacted state have been previously observed during the migration of breast epithelial cells in collagen microtracks with a high level of spatial confinement[16]. Furthermore, the intrinsic relationship between adopting a compacted mode and the increase in migration speed has been observed for other cell types in different confinement situations, such as migration on glass fibres with a diameter like that of the bridge width[17] (Extended Data Fig. 1a) or within collagen matrices[18] (Extended Data Fig. 1b).

High-resolution confocal microscopy (Fig. 2g and Supplementary Videos 6 and 7) revealed that elongated cells are larger, display a relatively uniform F-actin distribution along their length and contain a higher overall density of actin filaments (Fig. 2h,i) compared with compacted cells. Although some front–rear asymmetries can be observed—such as F-actin enrichment at the leading edge and a stem-like rear—the overall morphology remains less polarized than that of compacted cells. By contrast, compacted cells adopt a highly asymmetric shape characteristic of migrating cells, with a broad leading edge and a rounded rear (Fig. 2g, bottom), as well as significantly smaller spreading areas (Fig. 2h) and lower total actin filament density (Fig. 2i). Pronounced F-actin asymmetry in compacted cells (Fig. 2j) further reinforces their polarized morphology, a hallmark of fast migration[19].

To test the hypothesis that the difference in migratory dynamics between compacted and elongated cells may originate from a symmetry-breaking event in cell polarity, we explored a minimal biophysical model of active migration under confinement. Specifically, we modelled cells as polar particles exerting active migration forces in a direction of polarity $\mathbf{p} = (p_x, p_y)$. The dynamics of cell position $x(t)$ are then described by $\mathrm{d}x/\mathrm{d}t = p_x + F(x)$, where $F(x)$ is a repulsive force arising at the left and right edges of the micropattern to ensure confinement, which reflects the absence of ECM adhesion outside the adhesive track and ensures confinement consistent with the experimental set-up ('Theory note' in Supplementary Information). To describe the dynamics of cell polarity, we used a minimal model that allows both states in which cells are unpolarized (corresponding to morphologies with two opposing protrusions) and states in which cells are highly polarized in the direction of a single protrusion. Specifically, we hypothesized that the dynamics of cell polarity follow $\dot{\mathbf{p}} = (-\beta|\mathbf{p}|^2 - \alpha)\mathbf{p} + \gamma\mathbf{F}(x) + \sigma\boldsymbol{\xi}(t)$ with $\beta > 0$, where γ quantifies the tendency of cells to repolarize upon contact with the micropattern boundary, $\boldsymbol{\xi}(t)$ is Gaussian white noise that models fluctuations of the cell polarization and σ is the noise amplitude. Different states of polarization are determined by the parameter α. For positive α, the cell polarization stochastically fluctuates around a mean-zero polarization state (Fig. 2k, top). For negative α, the cell is highly polarized, with non-zero mean polarity (Fig. 2k, bottom). Simulations of our model with positive and negative α produced trajectories (Supplementary Video 8) that closely match those observed for elongated and compacted cell morphologies, respectively (Fig. 2l and Supplementary Video 3). On fitting α values to the experimentally measured crossing speeds, we indeed find positive and negative α for elongated and compacted cells, respectively ('Theory note' in Supplementary Information). Our model correctly captures that compacted cells were faster (Fig. 2m) and spend less time on the square islands between transitions, as quantified by the dwell time (Fig. 2n). Furthermore, our model captures key features of the qualitative nature of the nonlinear dynamics of elongated and compacted cells during their transit across the bridge. Elongated cells should exhibit a stable fixed point at vanishing speed $v = 0$, indicating that they are susceptible to stochastic fluctuations, leading to frequent changes in direction (Fig. 2o). Compacted cells exhibit two stable fixed points at finite speed, leading to a highly persistent crossing of the bridge at a fixed speed. These modelled dynamics can be measured experimentally by inferring the average acceleration of a cell as a function of its velocity for elongated and compacted cells[20] (Fig. 2p and 'Theory note' in Supplementary Information). This result confirms the hypothesized qualitative difference in nonlinear dynamics, with compacted cells exhibiting a pronounced separation of two stable fixed points at finite speeds $v \approx 2$ µm min^{-1}, closely matching the typical measured crossing velocity. Collectively, our findings demonstrate that compacted and elongated morphologies are associated with distinct migratory behaviours, governed by different polarization states under confinement.

To investigate molecular differences between polarization states, we analysed key markers involved in cell polarity, including vinculin-containing adhesion sites, Golgi positioning, β-tubulin distribution and Arp2/3 fluorescence intensity (Supplementary Video 9). Both elongated cells (Supplementary Fig. 3a) and compacted cells (Supplementary Fig. 3b) exhibited actin filament accumulation and vinculin-rich adhesions at the leading edge, primarily at the cell periphery.

https://doi.org/10.1038/s41567-025-02980-z

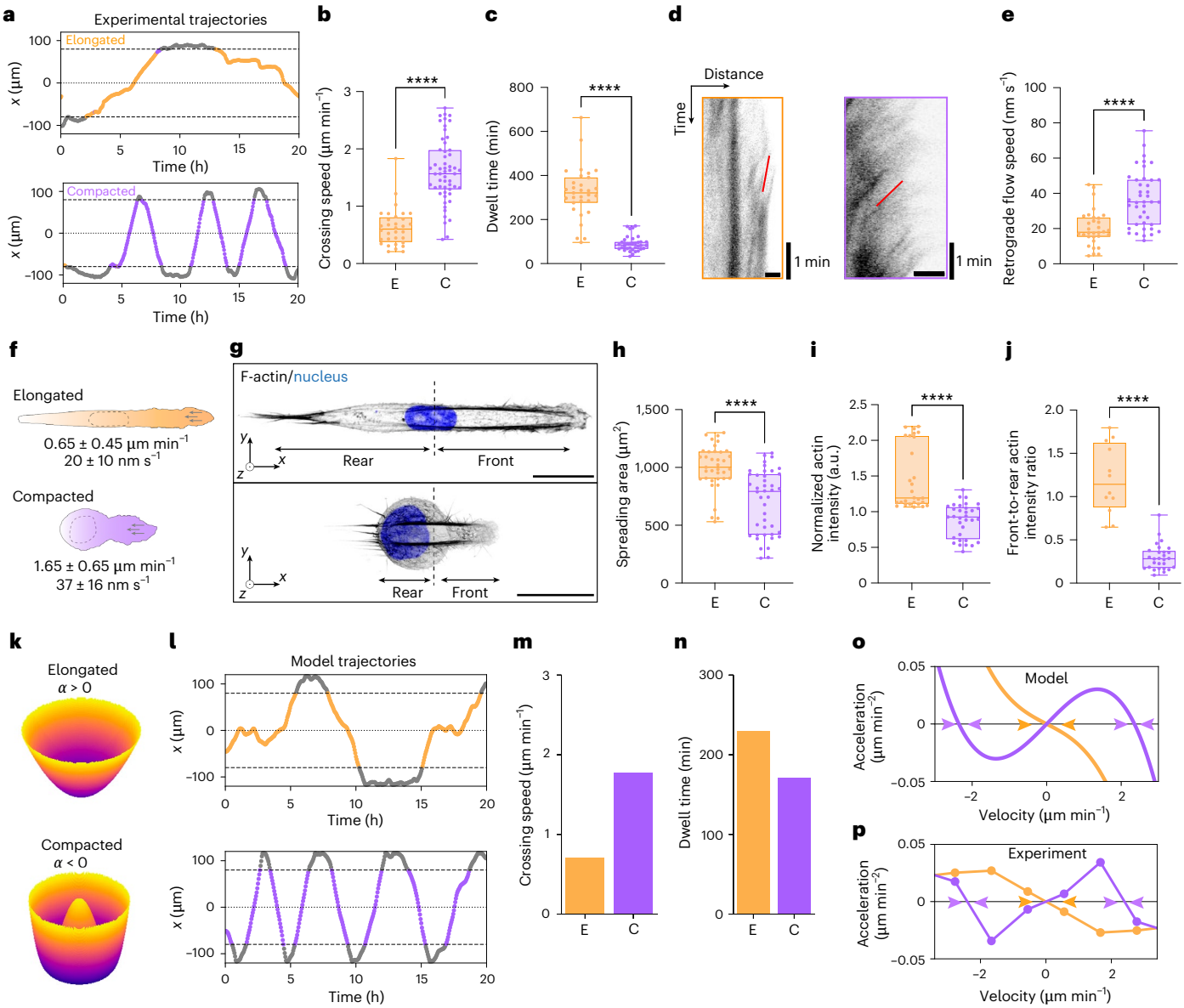

Fig. 2 | Impact of symmetry-breaking and polarization states on cell dynamics. **a**, Experimental trajectories for an elongated (top) and a compacted (bottom) cell morphology on a micropatterned dumbbell (160 µm long and 6 µm wide). Trajectories are colour-coded to show square zones (grey) and zones with elongated (orange, CSI < 0.4) or compacted morphologies (purple, CSI > 0.4). **b**,**c**, Crossing speed ($n = 32$ for elongated, $n = 55$ for compacted and $N = 16$) (**b**) and dwell time for elongated ($n = 31$ and $N = 16$) and compacted ($n = 36$ and $N = 16$) cell morphologies (**c**). **d**,**e**, Kymographs of the actin flow (**d**) and quantification of the retrograde actin flow speed (**e**) in the lamellipodia for elongated and compacted cells. **f**, Representative sketches of elongated ($n = 32$ and $N = 3$) and compacted ($n = 4$ and $N = 3$) morphologies with their associated mean cell speed and retrograde actin flow. Arrows show the direction of the retrograde flow. **g**, Representative confocal images in enhanced-resolution mode of elongated (top) and compacted (bottom) morphologies of MCF-10A cells. **h**, Spreading area ($n = 37$ for elongated, $n = 42$ for compacted and $N = 3$). **i**, Normalized actin intensity ($n = 28$ for elongated, $n = 33$ for compacted and $N = 3$). **j**, Front-to-rear actin intensity ratio ($n = 12$ for elongated, $n = 28$ for compacted and $N = 3$). **k**, Representation of cell polarity dynamics with $\alpha > 0$ when the cell polarization stochastically fluctuates around a zero-mean polarization state (top) and $\alpha < 0$ when the cell is highly polarized (bottom), with non-zero mean polarity. **l**–**n**, Representative trajectories (**l**), crossing speed (**m**) and dwell time (**n**) estimated by the model. Cell morphologies and time spent on squares are colour-coded. **o**,**p**, Average acceleration of elongated versus compacted cells as a function of the cell velocity as estimated by the model (**o**) and measured experimentally ($n = 57$ cells and $N = 16$) (**p**). Purple arrows show the presence of stable fixed points at finite speeds $v \approx 2$ µm min^{-1} close to experimental crossing speed values. Orange arrows show $v = 0$ where both curves cross each other. ****$P < 0.0001$ (Student's t-test or Kruskal–Wallis test). Box plots range from the first quartile to the third quartile, with the median (50th percentile) indicated by a line. Whiskers extend from the box to the minimum and maximum data points within 1.5 times the interquartile range. Scale bars, 2 µm (**d**), 20 µm (**g**, top), 25 µm (**g**, bottom).

This peripheral localization is consistent with a highly motile phenotype, where cells typically form smaller, more dynamic adhesion complexes. Adhesion sites were classified into three categories based on area[21]: nascent adhesions (<0.5 µm^2), focal complexes (0.5–1 µm^2) and focal adhesions (>1 µm^2). Elongated cells had comparable proportions of nascent adhesions and focal complexes but a lower frequency of focal adhesions. In contrast, compacted cells exhibited a higher proportion of nascent adhesions, a similar proportion of focal complexes and significantly fewer focal adhesions compared with elongated cells (Supplementary Fig. 3c,d).

The spatial distribution of adhesions was similarly front-biased in both morphologies, with 77.3 ± 16.7% in elongated cells and 82.0 ± 11.7%

in compacted cells (Supplementary Fig. 3e), with no statistically significant difference. The adhesive area at the front accounted for 2.3 ± 1.2% and 1.6 ± 0.9% of the total spreading area in elongated and compacted cells, respectively (Supplementary Fig. 3f). At the rear, this area was reduced to 1.0 ± 0.9% in elongated cells and 0.5 ± 0.3% in compacted cells (Supplementary Fig. 3g), a distribution consistent with that observed in fast-migrating phenotypes.

This observation aligns with previous studies of polarized migration on micropatterns[19,22], reinforcing the idea that compacted morphologies exhibit a higher degree of polarization. To further characterize these polarization states, we examined Golgi apparatus positioning, a well-established read-out of front–rear polarity during directed migration. In elongated, less polarized cells, the Golgi was typically positioned towards the leading edge, whereas in compacted, more polarized cells, it was relocated behind the nucleus (Supplementary Fig. 4a–d and Supplementary Video 9). This posterior positioning of the Golgi is characteristic of cells undergoing persistent migration and has been linked to enhanced directional stability. Supporting this, enhanced-resolution imaging revealed a strong accumulation of microtubules at the leading edge in compacted cells (Supplementary Fig. 4e), consistent with recent evidence that microtubule enrichment at the front is essential for maintaining persistent polarized migration[23].

In polarized cells, the Arp2/3 complex accumulates at the leading edge, where it nucleates branched actin networks that support lamellipodial protrusion; by contrast, reduced polarity is often associated with a diffuse cytoplasmic distribution of Arp2/3 ref. 24. To further evaluate front–rear polarity, we performed time-lapse imaging of MCF-10A cells expressing ArpC1B–mScarlet cultured on dumbbell-shaped micropatterns (Supplementary Fig. 4f,g). In compacted cells, Arp2/3 fluorescence was significantly enriched at the leading edge (Supplementary Fig. 4h), consistent with its well-established role in driving lamellipodial protrusion and maintaining directional migration[25]. We also analysed the temporal dynamics of Arp2/3 activity during back-and-forth migration events (Supplementary Fig. 5a and Supplementary Video 9). Notably, Arp2/3 fluorescence intensity increased significantly during morphological transitions from the elongated to the compacted state (Supplementary Fig. 5b and Supplementary Video 9), indicating a shift towards enhanced front–rear polarization.

Altogether, these findings demonstrate that compacted cells exhibit a higher degree of front–rear polarity compared with elongated cells, consistent with our theoretical model in which cells are modelled as active particles capable of adopting either a high-polarity (compacted) or low-polarity (elongated) state.

Dynamic morphological switch is controlled by local geometry

Importantly, single cells migrating in a confined environment can alternate between the elongated and compacted morphologies. This leads to morphological switch events during migration (Fig. 3a, Supplementary Fig. 6 and Supplementary Video 10), which are accompanied by an immediate change in migration speed, consistent with our previous results (Fig. 2b). This raises a central question: what are the statistical rules when cells switch between these two distinct morphological states? To gain insight into this, we analysed the evolution of cell shape over time during crossing events (Fig. 3b), using numerous experimental trajectories extracted from 20-h time-lapse videos. Based on the CSI, we automatically assigned in these trajectories the time spent in the elongated mode (orange), compacted mode (purple) and on the deconfinement squares (grey) (Fig. 3c). Interestingly, we found that the percentage of compacted cells, defined as having an average CSI on the bridge greater than 0.4 (Fig. 1d), strongly increased with the bridge length, reaching ~58% for a bridge length of 160 µm (Fig. 3d).

Previous theoretical work has indicated that the polarity dynamics of cells adapt to the local micropattern geometry[26,27], raising the question of whether a dependence of the dynamical switching on local confinement could explain the dependence of morphological states on bridge length. As a model with constant, fixed switching rate cannot capture the length dependence of compacted states ('Theory note' in Supplementary Information), we extended our model to include geometry-sensitive stochastic switching between elongated and compacted cells (Fig. 3e and Supplementary Video 8). Motivated by the idea that lateral confinement could drive shape adaptation in cells, we hypothesized that cells will more probably transition to a polarized ($\alpha < 0$), compacted, state when they are highly confined on the bridge and will more probably revert to an unpolarized ($\alpha > 0$), elongated state upon reaching the island. To model this, we assumed that the switching rates between the morphological states depend on the lateral width of the pattern (Fig. 3e and 'Theory note' in Supplementary Information): the transition rate from elongated to compacted $r_{E\to C}$ increases proportionally as the width decreases when the cell moves from the island into the confining bridge. Conversely, we assume that the rate of switching from compacted to elongated $r_{C\to E}$ increases proportionally with width when the cell exits the bridge and spreads onto the island. Although we cannot rule out more complex dependencies of the switching rates on the local width, such as different dependencies for compacted versus elongated cells, this provides a minimal model for the geometry-sensitive nature of the switch and was implemented through position-dependent switching rates $r_{E\to C}(x)$ and $r_{C\to E}(x)$, as illustrated in Fig. 3e and 'Theory note' in Supplementary Information.

This minimal model captured an increase in the percentage of compacted morphologies with bridge length (Fig. 3f), as observed experimentally (Fig. 3d). Furthermore, the model indicated that there was a further increase in the percentage of compacted cells in confining systems without islands (to 70%; Extended Data Fig. 2a). To test this, we confined cells to one-dimensional micropatterned lines 500 µm long (Extended Data Fig. 2b), and we analysed their shape during their back-and-forth motion (Extended Data Fig. 2c and Supplementary Video 11), finding an increase in the percentage of compacted cells (Extended Data Fig. 2d), in agreement with the outcome of the model. Together, these findings indicate that cells dynamically switch between elongated and compacted morphologies in a geometry-sensitive manner.

Cell memory links morphological states across transitions

We next investigated the overall timescales of the switching process. A key parameter in our model is the average time between switches T. If this time exceeds the average dwell time τ, the morphological state of cells in subsequent transitions is expected to be correlated. During any given transition, the probability of a cell being either elongated or compacted is 50% ($L = 160$ µm; Fig. 3g,h and Extended Data Fig. 3). In the absence of long-term memory ($T \ll \tau$), we expect these probabilities to be independent of the morphological state during the previous transition (Fig. 3h and 'Theory note' in Supplementary Information). By contrast, if $T > \tau$, cells will more probably remain in the same morphological state (Fig. 3h). Experimentally, we found strong correlations across transitions: after a compacted transition, 75 ± 5% of cells remained compacted in the subsequent transition, whereas 72 ± 6% of previously elongated cells retained their elongated state (Fig. 3g,h). By contrast, a memory-free process determined by the probabilities of the first passage would predict only 50 ± 5% retention. Similarly, the third consecutive transition also exhibits memory effects, with probabilities of 88 ± 6% for compacted cells and 78 ± 8% for elongated cells (Fig. 3g). These correlations across transitions are quantitatively captured by our model for a switching time $T \approx 2.3\tau \approx 10$ h. Given that the percentage of successful crossings was highest on 160-µm and 320-µm bridges (Fig. 1h) and that cells retain their morphological state across transitions across 160-µm bridges, we next investigated the memory process on 320-µm bridges by tracking cell morphology over time in

https://doi.org/10.1038/s41567-025-02980-z

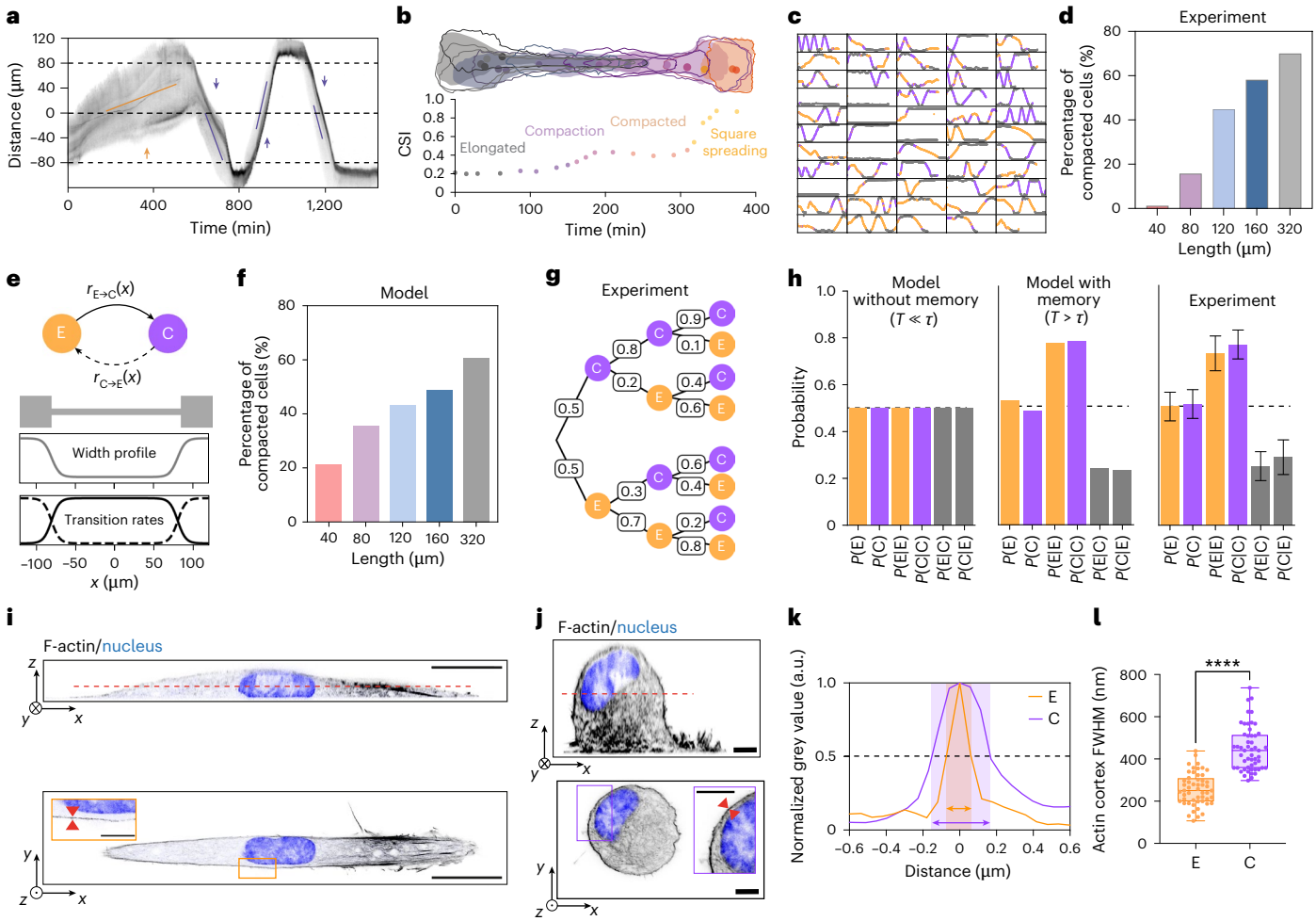

Fig. 3 | Morphological switch dynamics and mechanical memory. **a**, Representative kymograph of a migrating cell tagged for actin with SPY555-FastAct, showing a transition from an elongated to a compacted state over a 24-h time lapse. **b**, Representative colour-coded outline of an MCF-10A cell undergoing a morphological switch on a dumbbell micropattern, alongside the corresponding evolution of CSI versus time. **c**, Selection of colour-coded cell trajectories ($n = 55$ and $N = 11$) of individual MCF-10A cells migrating on FN dumbbell micropatterns for 20 h. Trajectories are colour-coded to represent square zones (islands; grey), elongated (CSI < 0.4, orange) and compacted (CSI > 0.4; purple) morphologies. **d**, Percentage of compacted cells for various bridge lengths ($n = 116$ for $L = 40$ μm, $n = 76$ for 80 μm, $n = 109$ for 120 μm and $n = 87$ for 160 μm, from $N \geq 3$). **e**, Sketch of the geometry-sensitive stochastic switching between elongated and compacted cells, including the spatial dependence of the normalized switching rates. **f**, Model estimates of the percentage of compacted cells for various bridge lengths. **g**, Statistical tree representation of the experimental probabilities for elongated and compacted states over three generations of successive crossings. **h**, Histogram representation of the probabilities for elongated $P(E)$ and compacted $P(C)$ states for various combinations of morphological switches: elongated to elongated $P(E \mid E)$, compacted to compacted $P(C \mid C)$, elongated to compacted $P(E \mid C)$ and compacted to elongated $P(C \mid E)$. Error bars represent the s.d. ($n = 55$ and $N = 11$). **i**,**j**, Confocal microscopy images in enhanced-resolution mode of side and top views of elongated (**i**) and compacted (**j**) cell morphologies. Inset: zoom-in showing the thickening of the actin cortex in compacted cells. **k**, Plot profile of the normalized actin intensity in the actin cortex for elongated and compacted cells. The light-purple zone indicates the distance corresponding to the full-width at half-maximum (FWHM) in compacted cells. **l**, FWHM for elongated ($n = 34$, E) and compacted ($n = 35$, C) cells. ****$P < 0.0001$ (Student's t-test, two-tailed, unequal variances). Box plots range from the first quartile to the third quartile, with the median (50th percentile) indicated by a line. Whiskers extend from the box to the minimum and maximum data points within 1.5 times the interquartile range. Scale bars, 20 μm (**i**), 5 μm (**j**).

50 time-lapse experiments, each lasting 35 h (Extended Data Fig. 4a). We used the CSI to automatically quantify, for each trajectory, the time spent in the elongated state (orange), in the compacted state (purple) and within the deconfinement zones (grey) (Extended Data Fig. 4b). As observed for 160-μm bridges, we found strong correlations across transitions (Extended Data Fig. 4c). Following a compacted transition, 71 ± 5% of cells remained compacted in the subsequent transition, whereas 60 ± 3% of previously elongated cells retained their elongated state (Extended Data Fig. 4d), in agreement with our model.

Together, these findings demonstrate that cells 'memorize' their morphological state across transitions. This raises a key question: how is this memory achieved, given that entry into the square is expected to lead to cell spreading and loss of polarization?

Compacted cells have a thicker actin cortex

To identify the origin of the long-term memory of short-term confining events over short periods of time, we first hypothesized that migrating cells can remodel their matrix by secreting ECM proteins. Therefore, we investigated the possibility that physicochemical footprints were left by cells during their migration, which could potentially result in history-dependent migration behaviours over an extended period[28]. We analysed the biochemical composition of the FN micropattern after 5 h of incubation with cells and at the end of the 20-h imaging period (Extended Data Fig. 5a) using immunostaining for pre-coated and cell-produced laminin (Extended Data Fig. 5b,c) as well as FN (Extended Data Fig. 5b–d). We found no statistical difference in FN or laminin intensity between the different

conditions, indicating that there is no direct relation to a biochemical remodelling of the surface.

We, therefore, hypothesized that the organization of the cytoskeleton could give rise to a mechanical memory across transitions. To test this, we used enhanced-resolution confocal microscopy to examine the architecture of the cytoskeleton, focusing on microtubules[23] and the actin cortex[29], which are key regulators of cell polarization and shape remodelling in confined environments. Microtubules were uniformly distributed in elongated cells and aligned along the bridge axis (Extended Data Fig. 6a). By contrast, compacted cells exhibited a striking redistribution of microtubules towards the rear (Extended Data Fig. 6b). Although both morphologies showed preferential microtubule alignment along the bridge axis at the front (Extended Data Fig. 6c), compacted cells displayed enhanced alignment along the vertical axis at the rear (Extended Data Fig. 6d), resulting in pronounced spatial asymmetry (Extended Data Fig. 6e). Surprisingly, we found that actin cortex organization also varied significantly between morphologies. Enhanced-resolution imaging of elongated (Fig. 3i and Supplementary Video 6) and compacted (Fig. 3j and Supplementary Video 7) morphologies revealed that the cortex thickness nearly doubled in compacted cells (Fig. 3k,l). This observation is consistent with recent findings indicating that cortex thickness regulates internal stress and cortical tension, thereby influencing cell shape[30]. Furthermore, it has been proposed that a deeper penetration of myosin filaments into the actin cortex of compacted cells could enhance the cortical tension in this state[31]. To explore this mechanism, we examined with enhanced-resolution microscopy the spatial distribution of pMLC at the actin cortex in elongated (Extended Data Fig. 7a,b) and compacted (Extended Data Fig. 7c,d) morphologies. In compacted cells, our results confirmed cortical thickening (Extended Data Fig. 7e) and revealed substantial colocalization with actin (Extended Data Fig. 7d), indicating increased myosin infiltration into the cortex. Together, these results support the idea that cortex thickening acts as a mechanical memory of previous confined events and, thus, stabilizes the compacted morphology over time.

Mechanical memory is controlled by the actin cortex

Assuming that mechanical memory is associated with reinforced front–rear polarity, microtubules and the actin cortex are probable candidates for explaining the origin of this mechanical memory. Indeed, it is well established that microtubules play a pivotal role in the establishment of cell polarity[32], whereas cortex thickening can stabilize the compacted cell shape, generate the propagation of long-range membrane tension[33] and, therefore, contribute to the maintenance of cell polarity[34]. To test these hypotheses, we first treated cells with nocodazole, which disrupts microtubule dynamics by binding to tubulin and leading to microtubule depolymerization (Extended Data Fig. 8a and Supplementary Video 12). Tubulin-treated cells exhibited a similar CSI on the bridge as control cells (Extended Data Fig. 8b), a similar area on squares (Extended Data Fig. 8c) but a very low rate of successful crossings (Extended Data Fig. 8d) and a very high dwell time (Extended Data Fig. 8e). Indeed, nocodazole-treated cells mostly became unable to migrate into the bridge and to maintain sufficient polarization to migrate within the confined area. Altogether, these results demonstrate that microtubules are not involved in the mechanical memory process related to maintaining the compacted shape but they are necessary for enabling the passage of epithelial cells in narrow environments.

In the next step, cells were treated either with a low concentration (20 nM) of latrunculin B (LatB; Fig. 4a–d and Supplementary Video 13) to weaken cortical F-actin or with Y27632 (Fig. 4e–h and Supplementary Video 14), which inhibits rho-associated protein kinase (ROCK), a key regulator of actin cortical tension, leading to a significant decrease in cortex elasticity[35]. Interestingly, the cortical tension was higher in cells with elevated ROCK activity compared with those with higher Rac1 activity, indicating that cortical tension increases when contractility dominates over actin polymerization[36]. We quantified back-and-forth cell movements during an initial 4-h control period, followed by another 20-h period after adding one of the pharmacological agents (Fig. 4b,f). Cells treated with LatB and Y27632 were significantly slower (Fig. 4c,g), exhibited a very low shape index on the bridge (Fig. 4d; CSI ≈ 0.2), which is characteristic of an extended morphology, and a much lower rate of successful passage (Fig. 4h). These findings collectively demonstrate the principal role of the actin cortex and the associated ROCK contraction pathway in maintaining the compacted shape.

Perturbing the mechanical memory dynamics

Our finding that the morphological states of cells on the confining bridge are correlated across transitions indicates that cells can retain a memory of their previous states during the periods of unconfinement on the square islands. Indeed, the spreading rate on the square islands (Extended Data Fig. 9a,b) can significantly affect the actin cortex thickness (Extended Data Fig. 9c) and, thus, perturb the mechanical memory. This raises the question of whether the two morphological states lead to distinct cytoskeletal organizations during the unconfining event on the islands. By studying transitions between two elongated shapes (E/E; Fig. 5a) or two compacted shapes (C/C; Fig. 5b), we observed that the cell area on squares of 1,600 μm^2 was statistically larger for E/E than for C/C (Fig. 5c), with a transition occurring at a cell area of around 1,000 μm^2. Additionally, we found that LatB- and Y27632-treated cells exhibited larger spreading areas (Fig. 5d) and longer dwell times (Fig. 5e) on squares compared with compacted cells. Interestingly, we observed a continuous decrease of CSI (Supplementary Fig. 7a,b) and crossing velocity (Supplementary Fig. 7c,d) after each crossing for LatB- and Y27632-treated cells, whereas the spreading area on squares increased continuously in both conditions (Supplementary Fig. 7e,f). Altogether, these results demonstrate that both the actin cytoskeleton and the ROCK contraction pathway control dwell times through cell spreading and actin cortex remodelling.

To test the role of available spreading area in the memory of morphological switching, we designed two new dumbbell geometries: (1) one with two squares of 900 μm^2, which is lower than the transition between morphological states observed around 1,000 μm^2 in (Fig. 5c), and (2) one with two squares of 2,500 μm^2, which are larger than the maximal spreading area after drug treatment (Fig. 5d). Conceptually, squares of 900 μm^2 constrain cells into a compacted state, whereas larger squares of 2,500 μm^2 provide the space for cells the transition into the elongated mode. By tracking back-and-forth motions on these new geometries (Fig. 5f and Supplementary Videos 15 and 16), we observed that the mean CSI on a bridge connected to 900 μm^2 squares (0.56 ± 0.16) was statistically larger than the mean CSI on a bridge connected to 1,600 μm^2 squares (0.44 ± 0.15), whereas cells migrating on dumbbells with 2,500 μm^2 squares exhibited a lower CSI (0.29 ± 0.12) (Fig. 5g), indicating that the larger the square, the lower the CSI on the bridge (Supplementary Fig. 8a). Furthermore, our results indicate that the percentage of compacted cells was very high on bridges connected to 900 μm^2 squares and decreased as the square area increased (Fig. 5h). Additionally, increasing the square area led to a proportional increase in dwell time (Fig. 5i and Supplementary Fig. 8b). We then expanded our model to reproduce the new dumbbell geometries and test its response to changes in the area of the squares. As shown in Fig. 5j,k, the model indicated that the larger the area of the square, the lower the proportion of compacted cells (Fig. 5j) and the longer the dwell time (Fig. 5k), consistent with our experimental observations, thereby supporting the validity of our model. Altogether, these results demonstrate that modulating the dwell time allowed us to tune the mechanical memory of confined cells.

https://doi.org/10.1038/s41567-025-02980-z

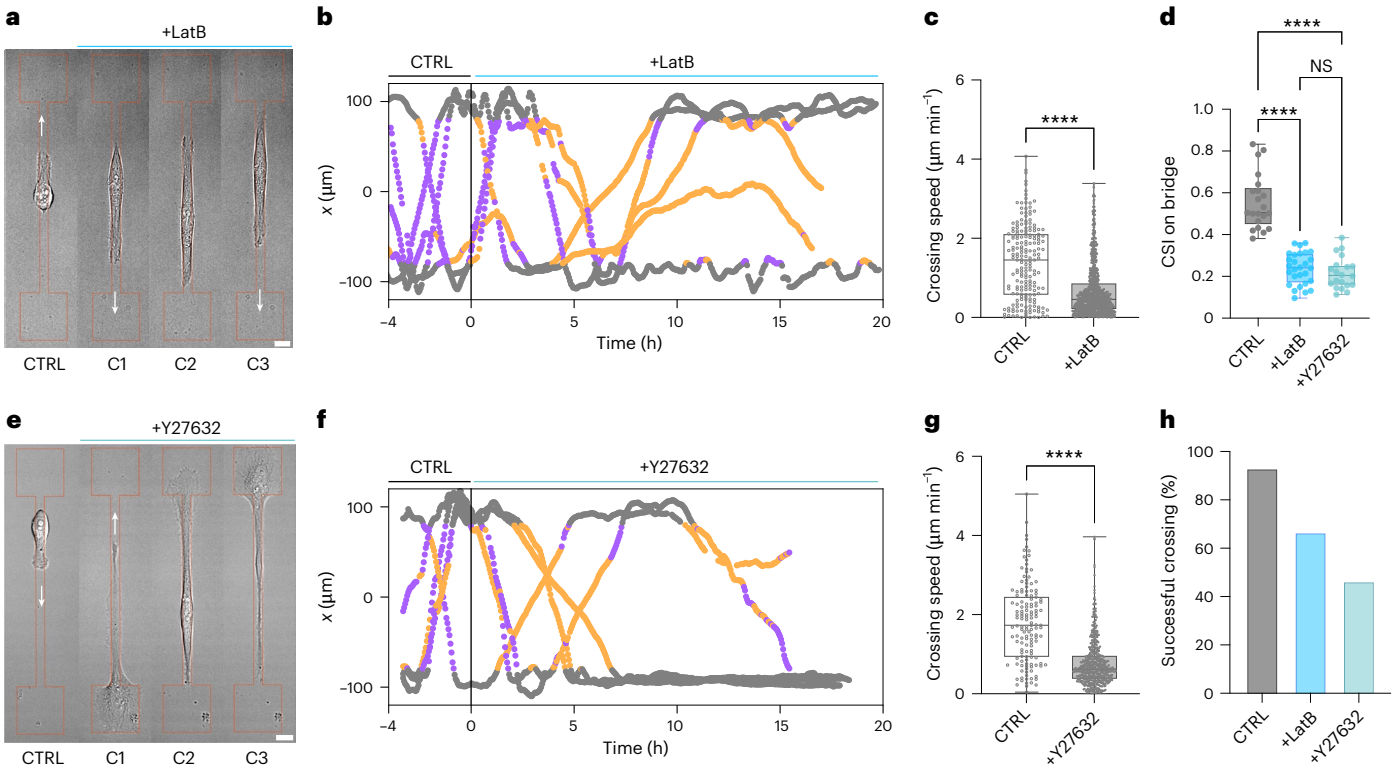

Fig. 4 | Pharmacological perturbation of mechanical memory dynamics. **a**, Sequence showing typical cell morphology during three successive crossings (C1, C2 and C3) after treatment with LatB. **b**, Representative trajectories of cells treated with LatB at $t = 0$ during their migration on a dumbbell pattern with a 160-µm-long bridge. Elongated morphologies, compacted morphologies and square zones (islands) are colour-coded as previously. The control was dimethyl sulfoxide (DMSO) for LatB. **c**, Mean crossing speed for cells before and after treatment with LatB ($n = 5$ and $N = 4$). **d**, CSI on bridge for control ($n = 21$) and LatB-treated cells ($n = 28$ and $N = 8$). **e**, Sequence showing typical cell morphology during three successive crossings (C1, C2 and C3) after treatment with Y27632. **f**, Representative trajectories of cells treated with Y27632 at $t = 0$ during their migration on a dumbbell pattern with a 160-µm-long bridge. Elongated morphologies, compacted morphologies and square zones (islands) are colour-coded. The control was water for Y27632. **g**, Mean crossing speed for cells before and after treatment with Y27632 ($n = 20$ for Y27632, $N = 8$). **h**, Successful crossing rate for control ($n = 146$), LatB ($n = 65$) and Y27632 ($n = 58$); $N \geq 8$ for all. ****$P < 0.0001$ (Student's t-test, two-tailed, unequal variances or Kruskal–Wallis test). Box plots range from the first quartile to the third quartile, with the median (50th percentile) indicated by a line. Whiskers extend from the box to the minimum and maximum data points within 1.5 times the interquartile range. CTRL, control group.

To demonstrate the crucial role of the actin cortex in maintaining cell-shape memory, we treated cells migrating on dumbbells connected to a deconfinement square of size 2,500 µm² with jasplakinolide (Jas; Supplementary Video 17), a pharmacological agent that stabilizes actin filaments. We used a moderate concentration of Jas, which has been shown to stabilize actin filaments and increase the actin cortex thickness[37] without significantly impacting the recycling of actin filaments in the lamellipodium, which is necessary for cell migration. Our results indicate that cells treated with Jas continued to migrate, adopted a more compacted shape (CSI = 0.51 ± 0.13; Fig. 5l) and exhibited a significantly shorter residence time ($\tau = 151 \pm 67$ min; Fig. 5m) than control cells. These results demonstrate that the reinforcement of the actin cytoskeleton enables cells to maintain a compacted shape even when placed in very large deconfinement areas that would typically lead to elongated shapes (Fig. 5g) and high residence times (Fig. 5i).

To determine the role of the mechanical memory in cells migrating through arrays of successive constrictions, we performed experiments on concatenated dumbbells, each featuring a deconfinement zone of either 900 µm² (Fig. 5n and Supplementary Video 18) or 2,500 µm² (Fig. 5o and Supplementary Video 18). These patterns allowed us to investigate the maintenance of mechanical memory as a function of the deconfinement zone size, thereby mimicking the successive confinement–deconfinement events experienced by cells as they migrate in a squeezed state within ECM fibres and in a more relaxed state through pores. These experiments revealed markedly different behaviours depending on the size of the relaxation zone: cells confined within 900 µm² patterns remain compact, directional and highly persistent. They crossed a series of ten interconnected motifs in less than 17 h (Fig. 5n). By contrast, cells on 2,500 µm² patterns were predominantly elongated, exhibited less persistent directional movement and struggled to traverse even a single motif over more than 60 h (Fig. 5o). Interestingly, the theoretical model accurately recapitulates key experimental features of elongated and compacted cell phenotypes migrating through complex 900 and 2,500 µm² successive patterns, such as the percentage of successful crossings (Extended Data Fig. 10a,b) and repolarization events (Extended Data Fig. 10c,d), thereby supporting the relevance and robustness of the model.

Discussion

Collectively, our data identify a morphological switch in confined migration and establish a mechanical memory function of the actin cortex. The dynamic switching between compacted and elongated morphologies allows cells to alternate between highly polarized, directed and more exploratory, undirected motility. This adaptability probably plays a key role in navigating through heterogeneous matrices and narrow constrictions, which is relevant to various physiological processes, such as immune cell patrolling, progenitor cell motility during development and cancer cell invasion.

https://doi.org/10.1038/s41567-025-02980-z

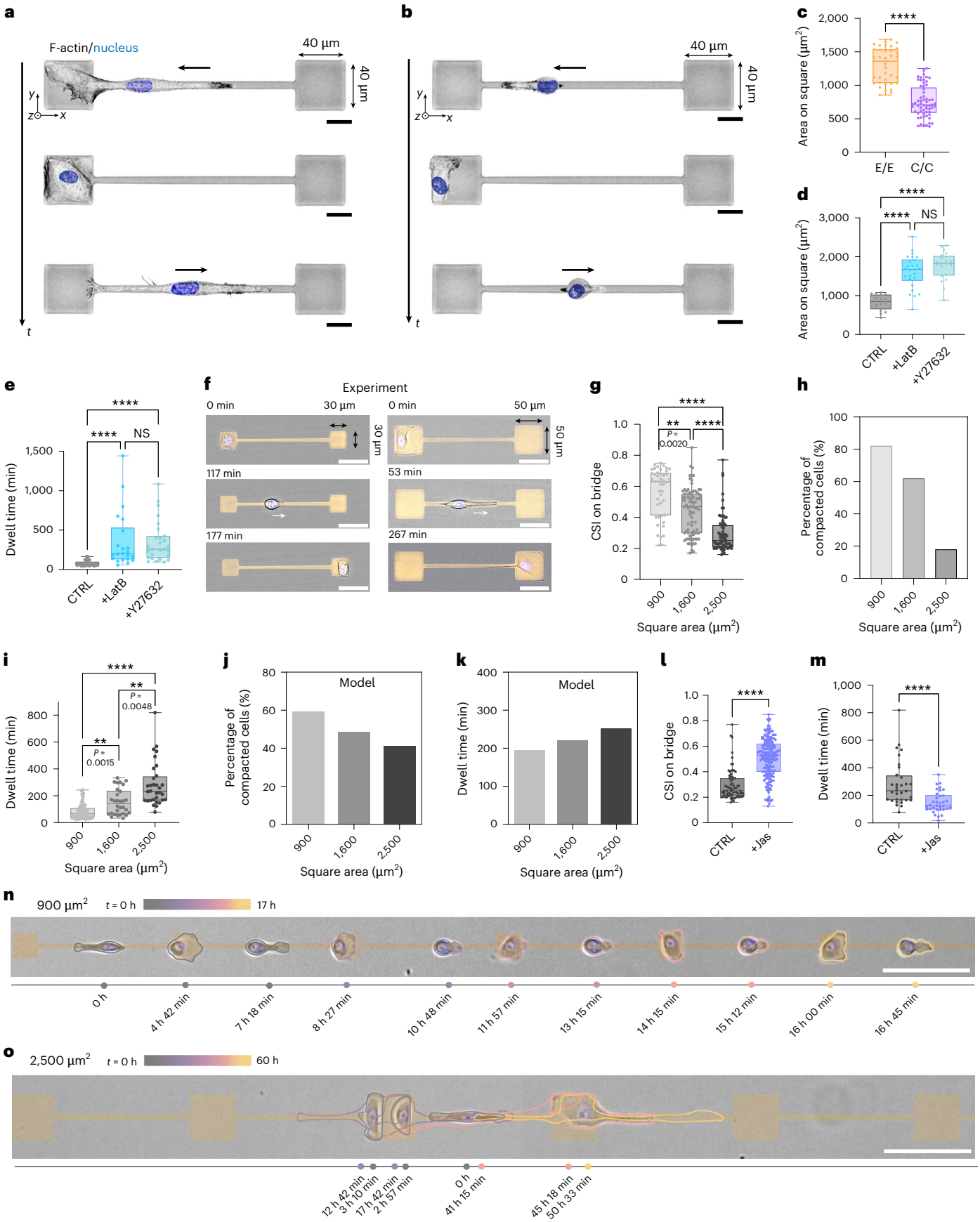

Fig. 5 | Geometrical perturbation of the mechanical memory dynamics. **a**,**b**, Representative sequence showing a transition between two elongated states (E/E) (**a**) and two compacted states (C/C) (**b**). **c**, Spreading area on 1,600 μm² squares during a transition between two elongated states (E/E, $n = 37$ and $N = 3$) and two compacted states (C/C, $n = 61$ and $N = 3$), indicating a transition around 1,000 μm². **d**,**e**, Mean cell area (**d**) and dwell time (**e**) on 1,600 μm² squares for control ($n = 27$ and $N \geq 4$), LatB-treated cells ($n = 22$ and $N \geq 4$), and Y27632-treated ($n = 27$ and $N \geq 4$) cells. **f**, Representative sequence showing a crossing event on a bridge ($L = 160$ μm and $W = 6$ μm) connected to squares of 900 μm² (left) and 2,500 μm² (right). **g**,**h**, CSI (**g**) and percentage (**h**) of compacted cells on a bridge 160 μm long and 6 μm wide for dumbbell geometries with squares of 900 μm² ($n = 45$ and $N = 3$), 1,600 μm² ($n = 87$ and $N = 14$) and 2,500 μm² ($n = 72$ and $N = 3$). **i**, Dwell time on squares of 900 μm² ($n = 45$ and $N = 2$), 1,600 μm² ($n = 87$ and $N = 16$) and 2,500 μm² ($n = 13$ and $N = 3$). **j**, Simulated behaviour of the percentage of compacted cells on a bridge 160 μm long and 6 μm wide for dumbbell geometries with squares of 900, 1,600 and 2,500 μm². **k**, Simulated behaviour of the dwell time on squares of 900, 1,600 and 2,500 μm². **l**, CSI for control cells ($n = 13$ and $N = 4$) and Jas-treated cells ($n = 207$ and $N = 4$). **m**, Dwell time for control cells ($n = 31$ and $N = 4$) and Jas-treated cells ($n = 34$ and $N = 4$, blue). The control was DMSO for Jas experiments. **n**,**o**, Representative time-lapse sequence of a single MCF-10A cell migrating on an interconnected dumbbell-shaped micropattern featuring 160-μm-long bridges and square deconfinement zones of 900 μm² (**n**) or 2,500 μm² (**o**). Colour-coded, time-dependent cell outlines are shown alongside. $^{***}P < 0.001$; $^{****}P < 0.0001$ (Student's t-test, two-tailed, unequal variances or Kruskal–Wallis test). Box plots range from the first quartile to the third quartile, with the median (50th percentile) indicated by a line. Whiskers extend from the box to the minimum and maximum data points within 1.5 times the interquartile range. Scale bars, 20 μm (**a**,**b**), 100 μm (**n**,**o**).

The mechanical memory we describe allows cells to retain a record of their previous morphological state, even as they transition through subsequent cycles of confinement and unconfinement. This memory is encoded by the organization of the actin cortex and enables cells to maintain a compacted morphology during temporary unconfinement events. The relationship between cortex thickness and mechanical properties is cell-type dependent. Although cortical thickening in oocytes has been associated with reduced cortical tension due to disproportionate actin polymerization over myosin contractility[38], our findings for MCF-10A epithelial cells align with previous reports indicating that cortex thickening correlates with increased cortical tension and enhanced migratory capacity[34]. Our findings support this epithelial-specific mechanism and highlight cortical thickening as a mechanical memory that sustains efficient migration under confinement. The retention of memory from previous confining events may allow cells to traverse heterogenous confinements such as interstitial spaces without having to pause to reorganize their shape each time they encounter an unconfined space. Notably this mechanical memory preserves a compacted, highly polarized state, which promotes rapid exploration through persistent motion and efficient navigation at dead ends. The bimodal transition between elongated and compacted morphologies arises from a coupling between confinement, actin cortex remodelling and polarity feedback. Increased confinement promotes front–rear polarization and cortex thickening, which reinforces the compacted state, whereas less-constrained regions allow more symmetrical spreading. This bistability is further enhanced by mechanical memory, as cells tend to maintain the compacted morphology even after leaving confinement, which enhances migratory efficiency.

From a theoretical perspective, our findings emphasize the complex time- and geometry-dependent dynamics of intrinsic active self-propulsion in migrating cells. Memory effects have previously been identified and modelled in the context of persistent single-cell migration on unconfined two-dimensional substrates[39,40] and one-dimensional lines[41], and it may also emerge in whole-cell simulation models[42–44]. However, the mechanical memory identified here governs morphological state transitions driven by confinement in structured environments, distinguishing it from previously studied migration memory effects. It would be interesting to investigate whether such memory emerges in whole-cell models of confined migration[45,46]. The observed morphological switch and its associated memory dynamics may also have notable implications for collective cell behaviour in confined environments, such as flocking transitions governed by the polarization state of cells. Although our focus here has been on identifying a minimal model to capture the long timescale statistics of morphological switches, future theoretical work will be needed to link these dynamics to mechanistic models of actin and polarity regulation[46–49].

To further elucidate the complex nature of this mechanical memory, key questions remain: how long must cells be confined for memory to be established? What are the changes in the three-dimensional nanostructure of the actin cortex that determine the timescale of the memory? Taken together, our findings represent among the most direct evidence to date that morphological switches enhance efficiency during confined migration and support the role of the actin cortex as a mechanoadaptive mechanism involved in maintaining in a cell the memory of past morphology during confined invasion.

Online content

Any methods, additional references, Nature Portfolio reporting summaries, source data, extended data, supplementary information, acknowledgements, peer review information; details of author contributions and competing interests; and statements of data and code availability are available at https://doi.org/10.1038/s41567-025-02980-z.

References

1. Jiang, C. Switch of cell migration modes orchestrated by changes of three-dimensional lamellipodium structure and intracellular diffusion. *Nat. Commun.* **14**, 5166 (2023).
2. Yang, C., Tibbitt, M. W., Basta, L. & Anseth, K. S. Mechanical memory and dosing influence stem cell fate. *Nat. Mater.* **13**, 645–652 (2014).
3. Nasrollahi, S. Past matrix stiffness primes epithelial cells and regulates their future collective migration through a mechanical memory. *Biomaterials* **146**, 146–155 (2017).
4. Lauffenburger, D. A. & Horwitz, A. F. Cell migration: a physically integrated molecular process. *Cell* **84**, 359–369 (1996).
5. Friedl, P. et al. Migration of coordinated cell clusters in mesenchymal and epithelial cancer explants in vitro. *Cancer Res.* **55**, 4557–4560 (1995).
6. Brückner, D. B. et al. Stochastic nonlinear dynamics of confined cell migration in two-state systems. *Nat. Phys.* **15**, 595–601 (2019).
7. Fink, A. et al. Area and geometry dependence of cell migration in asymmetric two-state micropatterns. *Biophys. J.* **118**, 552–564 (2020).
8. Brückner, D. B. et al. Learning the dynamics of cell–cell interactions in confined cell migration. *Proc. Natl Acad. Sci. USA* **118**, e2016602118 (2021).
9. Brückner, D. B., Ronceray, P. & Broedersz, C. P. Inferring the dynamics of underdamped stochastic systems. *Phys. Rev. Lett.* **125**, 058103 (2020).
10. Weigelin, B., Bakker, G.-J. & Friedl, P. Intravital third harmonic generation microscopy of collective melanoma cell invasion. *IntraVital* **1**, 32–43 (2012).
11. Ilina, O. et al. Cell–cell adhesion and 3D matrix confinement determine jamming transitions in breast cancer invasion. *Nat. Cell Biol.* **22**, 1103–1115 (2020).
12. Lee, J. W. N. & Holle, A. W. Engineering approaches for understanding mechanical memory in cancer metastasis. *APL Bioeng.* **8**, 021503 (2024).

13. Doyle, A. D., Wang, F. W., Matsumoto, K. & Yamada, K. M. One-dimensional topography underlies three-dimensional fibrillar cell migration. *J. Cell Biol.* **184**, 481–490 (2009).
14. Versaevel, M., Grevesse, T. & Gabriele, S. Spatial coordination between cell and nuclear shape within micropatterned endothelial cells. *Nat. Commun.* **3**, 671 (2012).
15. Maiuri, P. et al. Actin flows mediate a universal coupling between cell speed and cell persistence. *Cell* **161**, 374–386 (2015).
16. Mosier, J. A. et al. Extent of cell confinement in microtracks affects speed and results in differential matrix strains. *Biophys. J.* **117**, 1692–1701 (2019).
17. Yevick, H. G., Duclos, G., Bonnet, I. & Silberzan, P. Architecture and migration of an epithelium on a cylindrical wire. *Proc. Natl Acad. Sci. USA* **112**, 5944–5949 (2015).
18. Wang, W. Y., Davidson, C. D., Lin, D. & Baker, B. M. Actomyosin contractility-dependent matrix stretch and recoil induces rapid cell migration. *Nat. Commun.* **10**, 1186 (2019).
19. Hennig, K. et al. Stick-slip dynamics of cell adhesion triggers spontaneous symmetry breaking and directional migration of mesenchymal cells on one-dimensional lines. *Sci. Adv.* **6**, 5670 (2020).
20. Brückner, D. B. & Broedersz, C. P. Learning dynamical models of single and collective cell migration: a review. *Rep. Prog. Phys.* **87**, 056601 (2024).
21. Corne, T., Sieprath, T. & Vandenbussche, J. Deregulation of focal adhesion formation and cytoskeletal tension due to loss of A-type lamins. *Cell Adhes. Migr.* **11**, 447–463 (2017).
22. Pouthas, F. et al. In migrating cells, the Golgi complex and the position of the centrosome depend on geometrical constraints of the substratum. *J. Cell Sci.* **121**, 2406–2414 (2008).
23. Schmidt, C. J. Microtubule control of migration: coordination in confinement. *Curr. Opin. Cell Biol.* **86**, 102289 (2024).
24. Wu, C. et al. Arp2/3 is critical for lamellipodia and response to extracellular matrix cues but is dispensable for chemotaxis. *Cell* **148**, 973–987 (2012).
25. Pollard, T. D. & Borisy, G. G. Cellular motility driven by assembly and disassembly of actin filaments. *Cell* **112**, 453–465 (2003).
26. Flommersfeld, J., Stöberl, S., Shah, O., Rädler, J. O. & Broedersz, C. P. Geometry-sensitive protrusion growth directs confined cell migration. *Phys. Rev. Lett.* **132**, 098401 (2024).
27. Brückner, D. B. et al. Geometry adaptation of protrusion and polarity dynamics in confined cell migration. *Phys. Rev. X* **12**, 031041 (2022).
28. d'Alessandro, J. et al. Cell migration guided by long-lived spatial memory. *Nat. Commun.* **12**, 4118 (2021).
29. Chalut, K. J. & Paluch, E. K. The actin cortex: a bridge between cell shape and function. *Dev. Cell* **38**, 571–573 (2016).
30. Jawahar, A., Vermeil, J., Heuvingh, J., du Roure, O. & Piel, M. The third dimension of the actin cortex. *Curr. Opin. Cell Biol.* **89**, 102381 (2024).
31. Truong Quang, B. A. et al. Extent of myosin penetration within the actin cortex regulates cell surface mechanics. *Nat. Commun.* **12**, 6511 (2021).
32. Zhang, J., Guo, W.-H. & Wang, Y.-L. Microtubules stabilize cell polarity by localizing rear signals. *Proc. Natl Acad. Sci. USA* **111**, 16383–16388 (2014).
33. Belly, H. D. et al. Cell protrusions and contractions generate long-range membrane tension propagation. *Cell* **186**, 3049–3061 (2023).
34. Chugh, P. & Paluch, E. K. The actin cortex at a glance. *J. Cell Sci.* **131**, jcs186254 (2018).
35. Fritzsche, M. et al. Self-organizing actin patterns shape membrane architecture but not cell mechanics. *Nat. Commun.* **8**, 14347 (2017).
36. Bergert, M., Chandradoss, S. D., Desai, R. A. & Paluch, E. Cell mechanics control rapid transitions between blebs and lamellipodia during migration. *Proc. Natl Acad. Sci. USA* **109**, 14434–14439 (2012).
37. Clark, A. G., Dierkes, K. & Paluch, E. K. Monitoring actin cortex thickness in live cells. *Biophys. J.* **105**, 570–580 (2013).
38. Chaigne, A. et al. A soft cortex is essential for asymmetric spindle positioning in mouse oocytes. *Nat. Cell Biol.* **15**, 958–966 (2013).
39. Hakim, V. & Silberzan, P. Collective cell migration: a physics perspective. *Rep. Prog. Phys.* **80**, 076601 (2017).
40. Selmeczi, D., Mosler, S., Hagedorn, P. H., Larsen, N. B. & Flyvbjerg, H. Cell motility as persistent random motion: theories from experiments. *Biophys. J.* **89**, 912–931 (2005).
41. Mitterwallner, B. G., Schreiber, C., Daldrop, J. O., Rädler, J. O. & Netz, R. R. Non-Markovian data-driven modeling of single-cell motility. *Phys. Rev. E* **101**, 032408 (2020).
42. Brückner, D. B. & Hannezo, E. Tissue active matter: integrating mechanics and signaling into dynamical models. *Cold Spring Harb. Perspect. Biol.* **17**, a041653 (2025).
43. Ziebert, F. & Aranson, I. S. Computational approaches to substrate-based cell motility. *npj Comput. Mater.* **2**, 16019 (2016).
44. Shao, D., Rappel, W.-J. & Levine, H. Computational model for cell morphodynamics. *Phys. Rev. Lett.* **105**, 108104 (2010).
45. Sadhukhan, S. et al. Modeling how lamellipodia-driven cells maintain persistent migration and interact with external barriers. *Phys. Rev. Res.* **7**, 013319 (2025).
46. Marchetti, M. C., Joanny, J. F. & Ramaswamy, S. Hydrodynamics of soft active matter. *Rev. Mod. Phys.* **85**, 1143 (2013).
47. Ron, J. E., Monzo, P., Gauthier, N. C., Voituriez, R. & Gov, N. S. One-dimensional cell motility patterns. *Phys. Rev. Res.* **2**, 033237 (2020).
48. Zadeh, P. & Camley, B. A. Inferring nonlinear dynamics of cell migration. *PRX Life* **2**, 043020 (2024).
49. Sens, P. Stick-slip model for actin-driven cell protrusions, cell polarization, and crawling. *Proc. Natl. Acad. Sci. USA* **117**, 24670–24678 (2020).

Methods

Cell culture

MCF-10A cells were cultured in Dulbecco's modified Eagle's medium (Thermo Fisher, F-12) supplemented with 5% horse serum (Thermo Fisher), 20 ng ml^{-1} epidermal growth factor (Peprotech), 0.5 mg ml^{-1} hydrocortisone (Merck), 100 ng ml^{-1} cholera toxin (Enzo Life Sciences), 10 µg ml^{-1} insulin from bovine pancreas (Merck) and 0.1% penicillin/streptomycin (Merck). Cells were passaged every 3–4 days when reaching confluence and plated at a 1:4 dilution (~2 million cells per T75 flask). For cell passaging, the culture media was aspirated, and cells were washed with 10 ml of ×1 phosphate-buffered saline (PBS). After aspirating the PBS, cells were incubated with 2 ml of 0.25% trypsin (Merck) at 37 °C for 10 min. Trypsinization was halted by adding 4 ml of media, and cells were spun at 1.3 rpm for 5 min in a 15-ml Falcon tube to obtain a pellet. The old media was aspirated, and cells were resuspended in 1 ml of fresh media before being plated. MCF-10A cells were used for up to a maximum of 15 passages. To generate MCF-10A cells with endogenously tagged ARPC1B, we inserted the mScarlet fluorescent protein to the N terminal of ARPC1B using CRISPR genome editing. The donor plasmid consisted of homology arms, a hygromycin resistance gene, a self-cleaving T2A peptide and the mScarlet protein. Following electroporation of the cells with the sgRNA, the donor plasmid and a plasmid encoding Cas9 (Addgene 42230), cells were first selected with hygromycin (20 µg ml^{-1}) for 7–10 days before sorting with flow cytometry.

Immunocytochemistry and live staining

MCF-10A epithelial cells were fixed with 4% paraformaldehyde in PBS for 15 min at room temperature after cell migration experiments. Subsequently, cells were washed three times with PBS, with the last wash lasting for 5 min, and permeabilized using 0.05% Triton X-100 in PBS for 15 min at room temperature. After another round of three washes in PBS, permeabilized cells were blocked with a solution of 5 v/v% fetal bovine serum (Gibco) and 1 w/v% bovine serum albumin (Merck) in PBS for 30 min at room temperature. Actin filaments were stained with AlexaFluor 488 phalloidin (Invitrogen, 1:200), the nucleus with 4′,6-diamidino-2-phenylindole (DAPI; Invitrogen, 1:200) and microtubules with an anti-tubulin antibody produced in mouse (Sigma-Aldrich, 1:200). pMLC was stained using an anti-pMLC antibody in rabbit (Cell Signaling 3674, 1:200). For live labelling of the Golgi apparatus, cells were incubated overnight at 37 °C, 5% CO_2 using a CellLight Golgi-GFP BacMam 2.0 probe (Thermo Fisher C10592, 1:1,000). Following incubation, the cells were washed with PBS and the nucleus was stained with Hoechst (15 min at 1 µg ml^{-1}) before imaging.

Confocal microscopy

Images were collected in confocal mode with a motorized inverted microscope (Nikon A1R HD25) equipped with ×20, ×40, ×60 Plan Apo (numerical aperture 1.45, oil immersion) and ×100 Plan Apo silicone objectives and lasers that spanned the violet (405 and 440 nm), blue (457, 477 and 488 nm), green (514 and 543 nm), yellow-orange (568 and 594 nm) and red (633 and 647 nm) spectral regions. Confocal images were recorded with ×100 Plan Apo silicone objective of high numerical aperture (Plan Apochromat Lambda S ×100 Silicone, Nikon) in galvanometric mode with small Z-depth increments (0.1 µm) and a pinhole of 0.8 Airy unit (AU) to capture small cytoskeletal structures. Confocal images were recorded and processed using NIS-Elements (Nikon, Advanced Research v.4.5).

Enhanced-resolution confocal microscopy

The actin cytoskeleton and microtubule networks of MCF-10A cells were observed using confocal microscopy in enhanced-resolution mode. Images were captured using a confocal microscope (AX Ti2, Nikon) combined with the Nikon Spatial Array Confocal detector. Z-stack images were collected with a galvano scanner using a ×60/1.42 Plan Apo oil immersion objective and a step size of 0.17 µm for three channels (DAPI, TRITC and FITC). Confocal images were processed using the NIS-Elements software (Nikon, Advanced Research v.4.5), with a Richardson–Lucy deconvolution method applied to remove unfocused signals.

Time-lapse imaging

Back-and-forth motions on dumbbell micropatterns were recorded at ×40 magnification with a photometrics camera (Prime 95B, Photometrics Tucson) mounted on a motorized inverted microscope (A1R HD25 Ti2, Nikon). An incubation chamber (Okolab) was used to maintain CO_2 levels at 5% and the temperature at 37 °C throughout the imaging session. Time-lapse images were recorded for at least 20 h in differential interference contrast (DIC) and fluorescent modes with a time interval of 3 min and processed using NIS-Elements (Nikon, Advanced Research v.5.4).

F-Actin flow experiments

MCF-10A cells were incubated with SPY555-FastAct (Spirochrome) for 2 h at 37 °C following the manufacturer's protocol (dilution 1:1,000 in culture medium). Live actin imaging was performed in confocal mode on a motorized inverted microscope (A1R HD25 Ti2, Nikon) equipped with a Plan Apo ×100/1.35 silicone objective. An incubation chamber (Okolab) was used to maintain CO_2 levels at 5% and temperature at 37 °C throughout the imaging session. Images were acquired at a rate of one per 1.25 s for a total duration of 5 min. High-speed confocal images were recorded and processed using NIS-Elements (Nikon, Advanced Research v.5.4).

Determination of retrograde actin flow

To determine the retrograde actin flow at the cell leading edge (lamellipodium), time-lapse images were initially converted to 8-bit format, underwent background subtraction and contrast enhancement, and were subjected to a Gaussian blur filter (sigma = 1.5). Subsequently, kymographs were generated using the reslice command tool in Fiji. Kymographs were obtained from 1-pixel-wide lines drawn at the centre of the lamellipodia. Three lines were drawn per lamellipodia and the xy coordinates of each line was saved to calculate the slope corresponding to the flow speed in units of micrometres per second, which was subsequently converted to nanometres per second:

$$v = \frac{x_2 - x_1}{t_2 - t_1}.$$

Actin fluorescence analysis

To quantify the intensity of actin filaments in migrating cells, we proceeded as follows. Time-lapse images of MCF-10A cells stained with SPY555-FastAct were first converted to 8-bit format, then thresholded, binarized, and analysed using the Particle analysis tool in Fiji. The background intensity was measured outside threshold areas using the same approach and subtracted from the raw cell intensity. For a cell entirely located on the bridge—whether in an elongated or compacted state—the fluorescence intensity was normalized to the average fluorescence intensity of the same cell in the square areas at each end of the dumbbells. This normalization allowed us to account for signal variability between the different cells analysed.

Protein micropatterning

To ensure precise control over protein density, micropatterns were not fabricated using the conventional microcontact printing method[50–53] but instead by light-induced molecular adsorption of protein using the Primo system (Alvéole) on glass substrates, as previously described[54]. Briefly, glass-bottomed dishes (Cellvis) and polydimethylsiloxane stencils were plasma-activated for 3 min (Harrick Pasma) before their assembly. The stencils allowed to minimize the volume of the solution and avoid fast dewetting of the surface. The glass surface was coated using a 0.1% (m/v) poly-L-lysin for 30 min at room temperature and

incubated for 1 h at room temperature with a 100 mg ml^{-1} passivation solution of polyethylene glycol-succinimidyl valerate. After drying, the surface was covered with a mixture of PLLP-gel photo-initiator solution (Alvéole), surfactant and 70% ethanol and left to dry for 30 min before being transferred to the microscope stage. Designed motifs were projected onto glass through a Primo Digital Micromirror Device using Leonardo software (Alvéole). A dose of 100 mJ mm^{-2} at 375-nm ultraviolet light illumination (100% laser power) focused through a ×20 objective (Nikon, Plan Fluor) was used to activate the photo-initiator and remove the passivation layer at desired locations. The surface was washed and coated with 15 µg ml^{-1} human plasma FN (Sigma) containing 5 µg ml^{-1} of fluorescent human plasma FN for 5 min at room temperature. Patterned surfaces were either used directly or stored at 4 °C in 0.1 M $NaHCO_3$ buffer (pH = 8.3) for up to 24 h after preparation.

Drug treatments

Actin depolymerization, ROCK inhibition and microtubule depolymerization treatment were achieved upon addition of 20 nM LatB, 10 µM Y27632 or 2.5 µM nocodazole, respectively, to samples after 4 h of time-lapse imaging. Then imaging was resumed for another 20 h in the presence of the drug. Actin stabilization treatments were performed by incubating samples with 1 nM of Jas 30 min before the beginning of the time-lapse experiments. LatB, nocodazole and Jas were diluted in DMSO, whereas Y27632 was diluted in water.

Cell tracking

Time-lapse sequences were recorded for 20 h in DIC mode with a time interval of 3 min, leading to approximately 400 frames per experiment. Cell trajectories were tracked using time-lapse imaging for different bridge lengths. Cell segmentation was performed using Cellpose 2.0 (ref. 55), a deep learning-based tool, integrated into TrackMate (Fiji) for automated tracking. The full cell contour was segmented from DIC sequences, manually verified and analysed to extract cell spreading area, perimeter and the coordinates of the cell front, rear and centre of mass. A passage was classified as failed if the cell changed direction before its centre of mass had reached the opposite square area. A successful passage was defined as a complete traversal of the bridge, with the centre of mass reaching the opposite square area.

Cell shape index

Areas (A) and perimeters (P) of migrating cells were measured for DIC images with ImageJ using CellPose 2.0. Both geometrical parameters were used to calculate the CSI from the relation:

$$\mathrm{CSI} = \frac{4\pi A}{P^2}.$$

The CSI assumes values between 1 (circular shape) and 0 (elongated, linear morphology).

Physicochemical footprints

Given that the physicochemical footprints left by migrating cells over an extended period can influence their migration speed and trajectory[28], we analysed the biochemical composition of the FN micropattern after 5 h of cell incubation and at the end of the 20-h imaging period. Samples were fixed at two time points—early (t = 5 h) and late (t = 24 h)—and immunostained for pre-coated and cell-produced laminins (anti-laminin produced in rabbit, Sigma-Aldrich L9393) as well as FNs, with a specific antibody recognizing cell-derived FN (anti-IST9 fibronectin, Santa Cruz Biotechnology). We strictly followed the protocol for immunostaining and analysis of the immunostained conditioned substrates previously described[28], without any modifications.

Statistical analysis

Each experiment was repeated at least three times. Each dataset was tested for normality test using the d'Agostino–Pearson test in Prism v.10 (GraphPad Software), which combines skewness and kurtosis tests to determine whether the shape of the data distribution resembled the shape of a normal distribution. For paired comparisons, significances were calculated in Prism v.10 (GraphPad Software) with Student's t-test (two-tailed, unequal variances) when the distributions proved to be normal. If a dataset did not pass the normality tests, the significances were calculated with a Mann–Whitney test (two-tailed, unequal variances). For multiple comparisons with non-normal distribution, datasets were analysed with a Kruskal–Wallis test in Prism v.10 (GraphPad Software), which is a suitable non-parametric test for comparing several independent groups when the data are skewed. When the null hypothesis was not retained ($P < 0.05$), the Kruskal–Wallis test was corrected with Dunn's test, which is a non-parametric test with no pairing and multiple comparisons that can be used for both equal and unequal sample sizes. Unless otherwise stated, all data are presented as mean ± s.d. Box plots were generated using Prism v.10 (GraphPad Software). In all box plots, the central line represents the median, the box boundaries indicate the 25th and 75th percentiles (interquartile range), and whiskers extend to the minimum and maximum values excluding outliers. The confidence interval in all experiments was 95%, and as a detailed description of statistical parameters, it is included in all figure captions with $^*P < 0.05$, $^{**}P < 0.01$, $^{***}P < 0.001$ and $^{****}P < 0.0001$.

Error analysis of conditional morphological state probabilities

To calculate error bars on the transition probabilities between morphological states, we employed a bootstrapping procedure[56]. Briefly, from our dataset of N cell trajectories $\{x_k\}$, where $k = 1, \ldots, N$, we generated M = 1,000 bootstrap realizations by randomly sampling N cell pair trajectories with replacement for each realization. To obtain the error in a transition probability measured from the experimental dataset, we estimated the value of this probability for each bootstrap realization and took the s.d. of all obtained probabilities as our estimate for the error in the estimate of this probability.

Reporting summary

Further information on research design is available in the Nature Portfolio Reporting Summary linked to this article.

Data availability

All data are available upon request to the corresponding authors. Source data are provided with this paper.

Code availability

Codes are available upon request to D.B.B.

References

50. Grevesse, T., Versaevel, M., Circelli, G., Desprez, S. & Gabriele, S. A simple route to functionalize polyacrylamide hydrogels for the independent tuning of mechanotransduction cues. *Lab Chip* **13**, 777 (2013).
51. Grevesse, T., Versaevel, M. & Gabriele, S. Preparation of hydroxy-PAAm hydrogels for decoupling the effects of mechano-transduction cues. *J. Vis. Exp.* **28**, 51010 (2014).
52. Vercruysse, E. et al. Geometry-driven migration efficiency of autonomous epithelial cell clusters. *Nat. Phys.* **20**, 1492–1500 (2024).
53. Ciccone, G. et al. Epithelial cell mechanoresponse to matrix viscoelasticity and confinement within micropatterned viscoelastic hydrogels. *Adv. Sci.* **12**, 2408635 (2025).
54. Strale, P.-O. et al. Multiprotein printing by light-induced molecular adsorption. *Adv. Mater.* **28**, 2024–2029 (2016).
55. Stringer, C., Wang, T., Michaelos, M. & Pachitariu, M. CellPose: a generalist algorithm for cellular segmentation. *Nat. Methods* **18**, 100–106 (2021).
56. Efron, B. Bootstrap methods: another look at the jackknife. *Ann. Stat.* **7**, 1–26 (1979).

Acknowledgements
We are grateful to members of S.G.'s laboratory for feedback and suggestions. We thank E. Hannezo, J. O. Rädler, M. Piel, O. du Roure and J. Heuvingh for inspiring discussions. Y.K. and S.G. acknowledge J. B. Braquenier from Nikon Instruments Belux and the Nikon BioImaging Lab in Leiden (the Netherlands) for their support with the Nikon Spatial Array Confocal enhanced-resolution confocal microscopy. We thank D. S. Herrador and M. Balland for their help in improving the microprinting method. D.B.B. was supported by the NOMIS Foundation as a NOMIS Fellow and by an EMBO Postdoctoral Fellowship (ALTF 343-2022). Y.K., M.L. and S.G. acknowledge funding from the University of Mons (FEDER Prostem Research Project no. 1510614, Wallonia DG06), the F.R.S.-FNRS (Epiforce Project no. T.0092.21, Cellsqueezer Project no. J.0061.23 and Optopattern Project no. U.NO26.22) and the Interreg projects ANTIRESI and MICROPLAITE, which are financially supported by Interreg France-Wallonie-Vlaanderen (Fonds Européen de Développement Régional). Y.K. and M.L. are financially supported by F.R.S.-FNRS as FRIA Grantee FNRS and Postdoctoral Fellow (Chargé de Recherches), respectively. Y.K. and S.G. acknowledge le Fonds pour la Recherche Médicale dans le Hainaut (FRMH). G.C. was supported by a grant from the Biotechnology and Biological Sciences Research Council (grant no. BB/V007483/1).

Author contributions
S.G. and Y.K. conceived of the project, and S.G. supervised the project. Y.K. developed the micropatterns and performed the time-lapse cell experiments, cell tracking and confocal imaging. D.B.B. developed the theoretical model and performed the simulations. M.L. contributed to the experiments and commented on the paper. G.C. provided cell lines and commented on the paper. G.S. conceived of the Arpc1b MCF-10A cell line. Y.K., D.B.B. and S.G. analysed the data and prepared the figures. The article was written by Y.K., D.B.B. and S.G. and read and corrected by all authors, who each contributed to the interpretation of the results.

Competing interests
The authors declare no competing interests.

Additional information
Extended data is available for this paper at https://doi.org/10.1038/s41567-025-02980-z.

Supplementary information The online version contains supplementary material available at https://doi.org/10.1038/s41567-025-02980-z.

Correspondence and requests for materials should be addressed to David B. Brückner or Sylvain Gabriele.

Peer review information *Nature Physics* thanks Falko Ziebert and the other, anonymous, reviewer(s) for their contribution to the peer review of this work.

https://doi.org/10.1038/s41567-025-02980-z

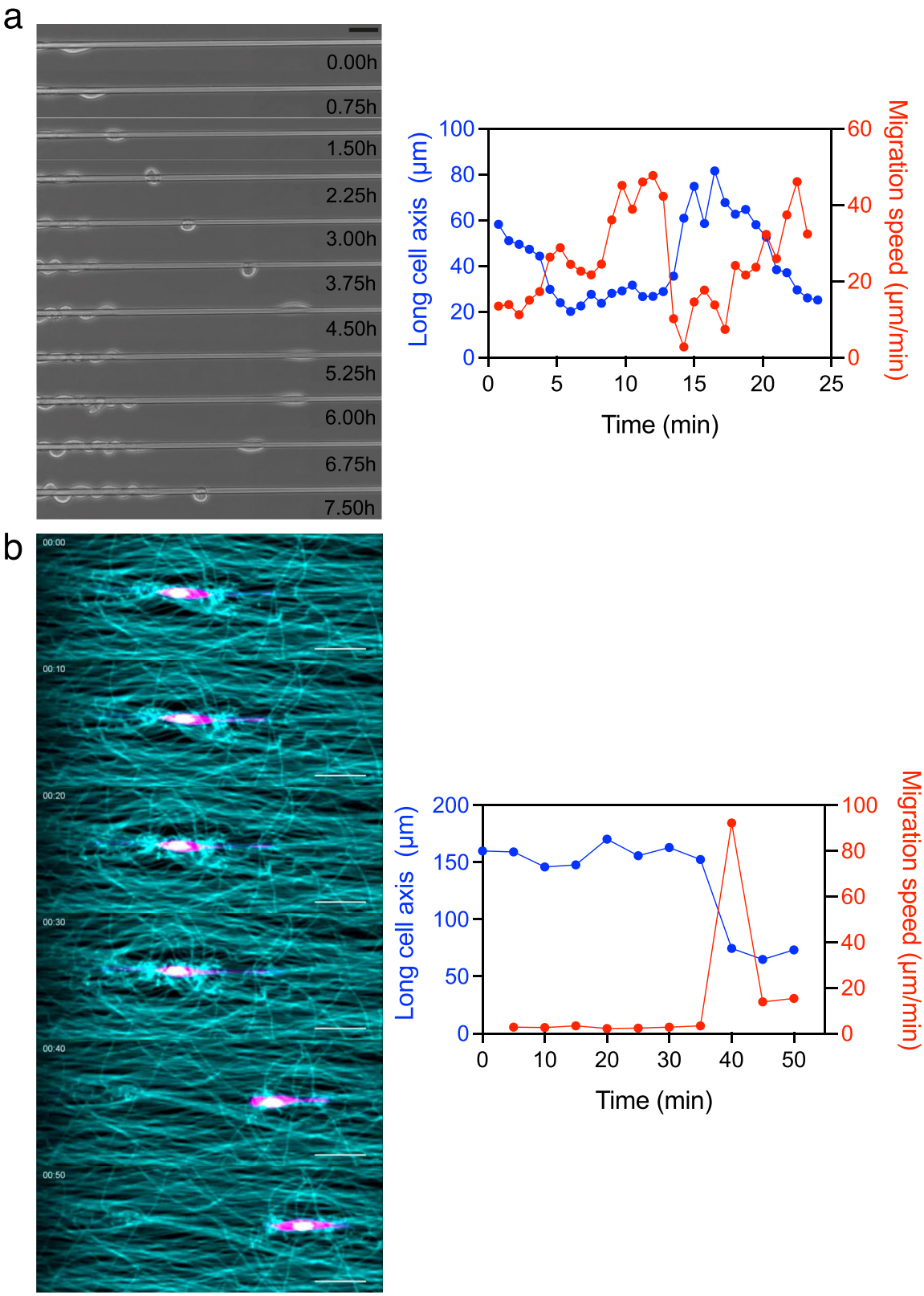

Extended Data Fig. 1 | Examples of morphological switch on glass fiber and in 3D collagen fiber matrix. (**a**) Time-lapse sequence of a single MDCK epithelial cell migrating on a smooth glass wire (diameter = 5.3 μm). After detaching from the tissue, the epithelial cell rounds up and migrate on the glass fiber. The temporal evolution of the long cell axis and the migration speed indicates that the cell morphological switch from an elongated to a compacted morphology is associated with an increase in migration speed. Scale bar, 50 μm. Adapted with permission from **17**. (**b**) Time-lapse sequence of a single fibroblast (NIH3T3) migrating in a 3D matrix composed of aligned collagen fibers. Scale bar, 50 μm. The temporal evolution of the long cell axis and the migration speed indicates that the cell morphological switch from an elongated to a compacted morphology is associated with an increase in migration speed with a maximum speed around 80 μm/min. Adapted with permission from **18**.

https://doi.org/10.1038/s41567-025-02980-z

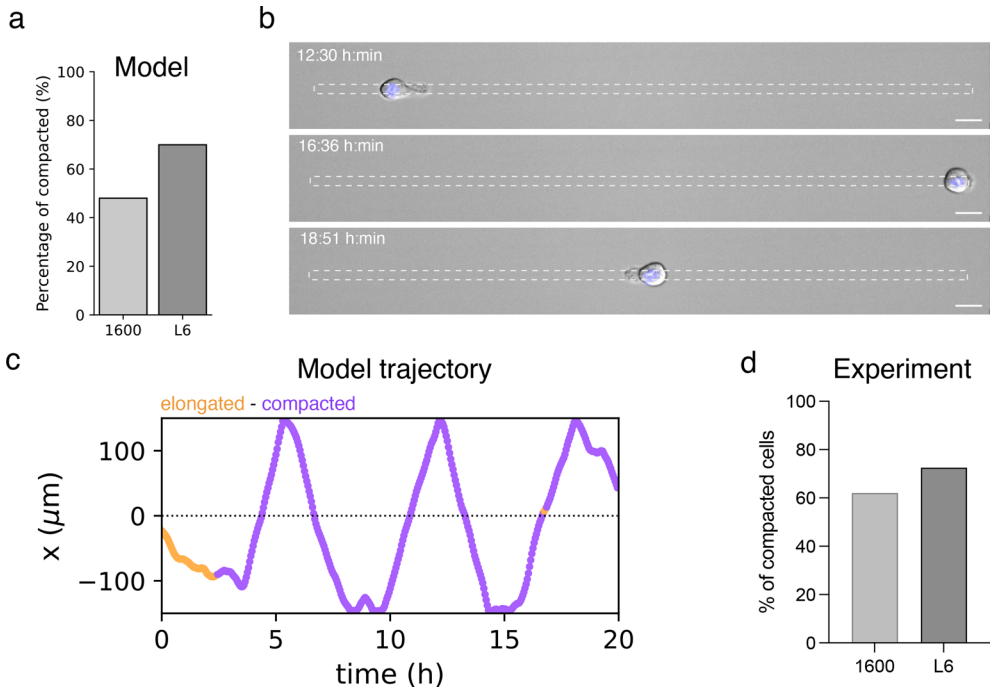

Extended Data Fig. 2 | Semi-infinite narrow segments. (**a**) Theoretical expectation of the percentage of compacted cell on the bridge of dumbbells (W = 6 µm and L = 160 µm) with square area of 1600 µm^2 versus 1D semi-infinite line of W = 6 µm and L = 500 µm. On 6 µm line, percentage of compacted cell is expressed as the percentage of time spent under the compacted morphology over a 20-hour time-lapse. (**b**) Time-lapse sequence of a compacted cell morphology migrating on a one-dimensional (1D) micropatterned line of W = 6 µm and L = 500 µm. Scale bar, 20 µm. (**c**) Representative color-coded trajectories with elongated (CSI < 0.4) and compacted (CSI > 0.4) morphologies. (**d**) Percentage of compacted cells on the bridge of dumbbells (W = 6 µm and L = 160 µm) with square area of 1600 µm^2 (n = 56, N = 16) versus 1D semi-infinite line of W = 6 µm and L = 500 µm (n = 10, N = 2). On 6 µm line, percentage of compacted cell is expressed as the percentage of time spent under the compacted morphology over a 20-hour time-lapse.

https://doi.org/10.1038/s41567-025-02980-z

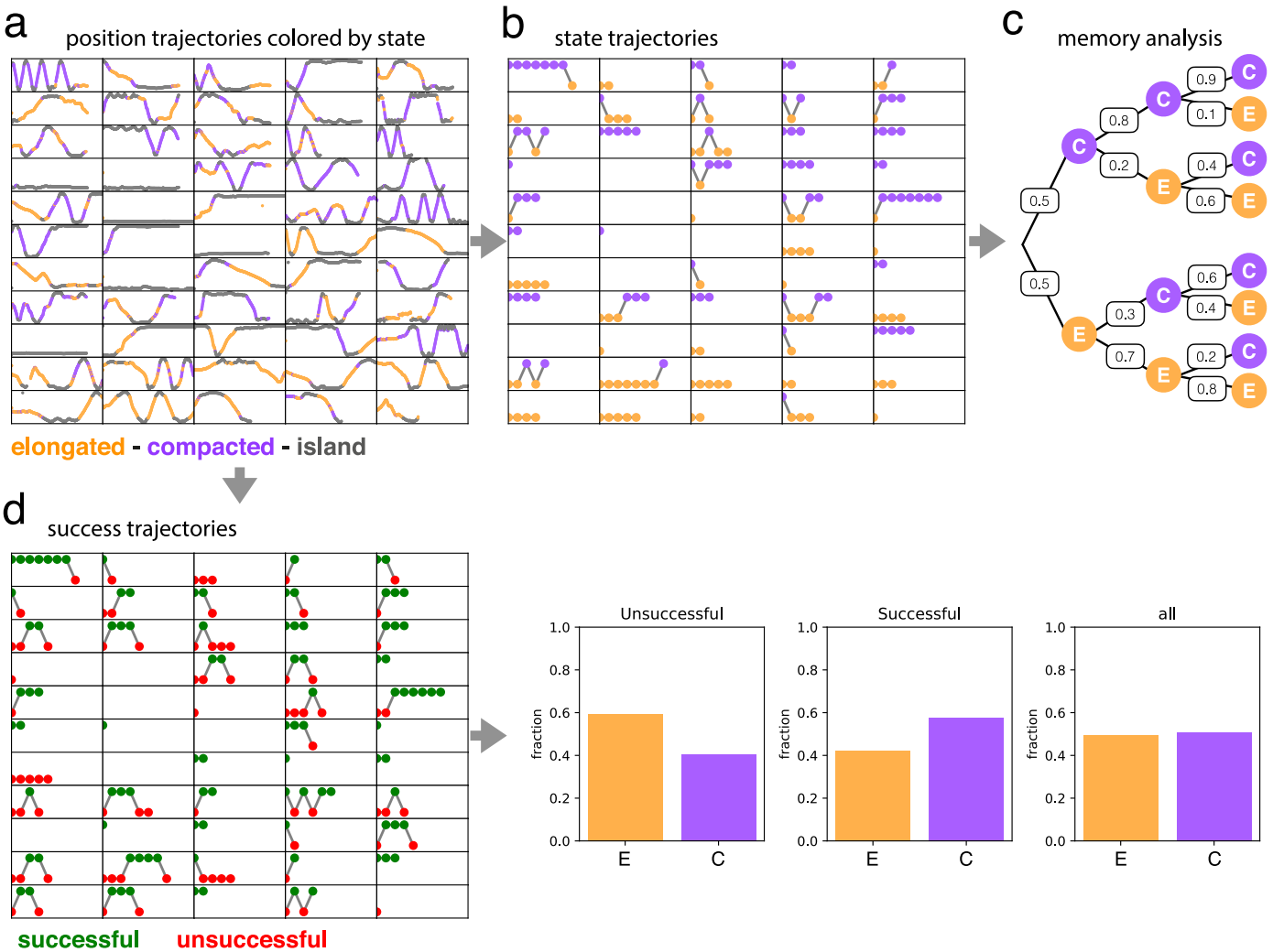

Extended Data Fig. 3 | Analysis of memory dynamics from cell trajectories. (**a**) Selection of n = 55 color-coded single cell trajectories of individual MCF-10A cells migrating on FN dumbbell micropatterns for 20 hours. Trajectories on the bridge are color-coded by state: elongated (CSI < 0.4) and compacted (CSI > 0.4) morphologies. (**b**) State trajectories computed from position trajectories in (A). A morphological state is assigned to each transition on the bridge, based on the morphological state adopted for most time-points during each transition. (**c**) Memory analysis tree diagram for events C (compacted transition) and E (elongated transition) obtained from state trajectories in (b). Numbers of the branches indicate probabilities. (**d**) Trajectories of successful and unsuccessful transitions, defined as follows: in successful transitions, the cell (nucleus) enters the bridge and transmigrates to the other island. In unsuccessful transitions, the nucleus enters the bridge and returns to the same island. Fraction of unsuccessful, successful and total transition, which are repartitioned into two categories, elongated and compacted.

https://doi.org/10.1038/s41567-025-02980-z

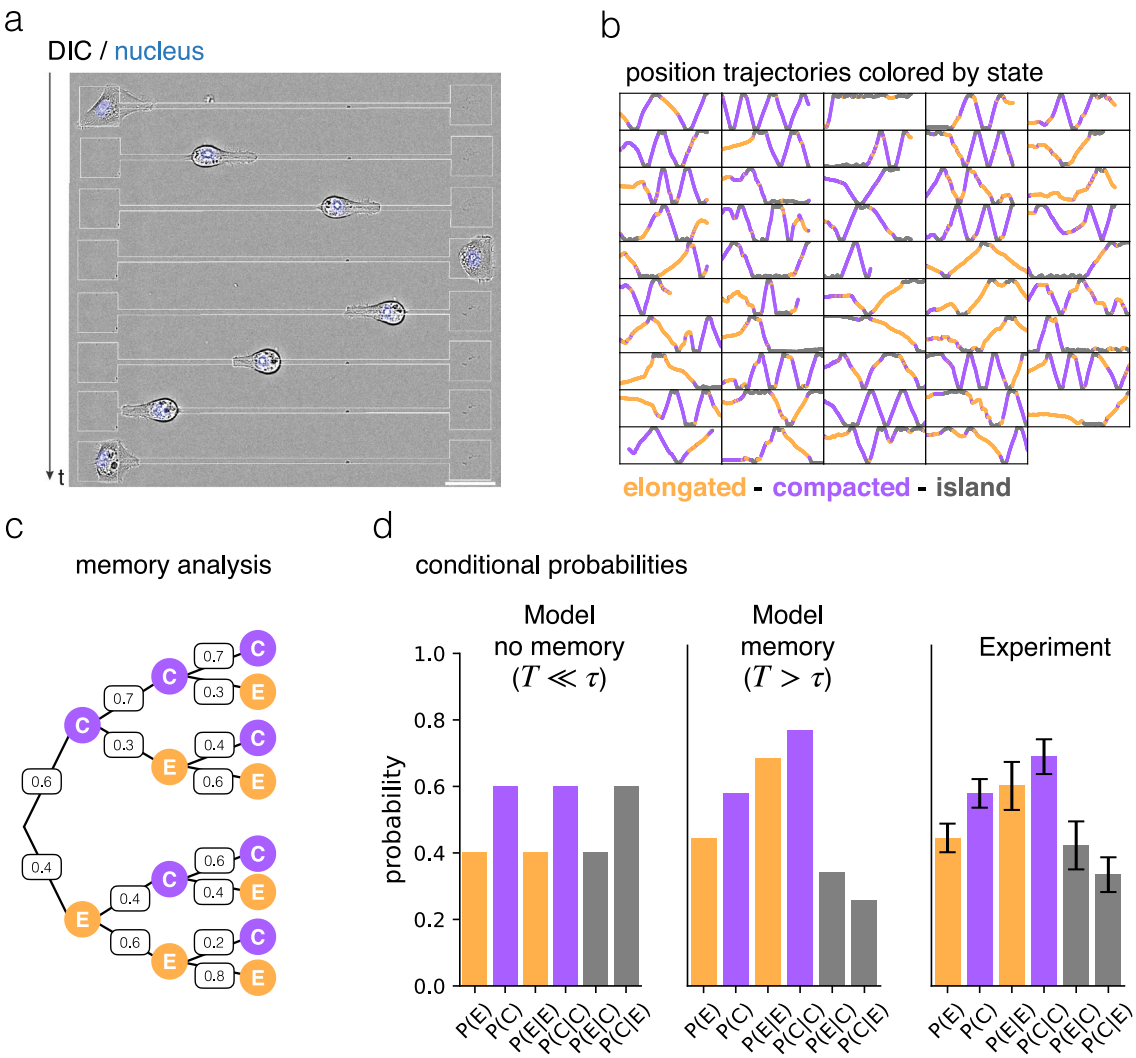

Extended Data Fig. 4 | Morphological switching dynamics and mechanical memory on 320 µm-long bridges. (**a**) Representative sequence of a back-and-forth motion of an individual MCF-10A cell migrating on an FN dumbbell micropattern with a 320 µm-long bridge. (**b**) Selection of n = 50 color-coded cell trajectories of individual MCF-10A cells migrating on FN dumbbell micropatterns for 30 hours. Trajectories on the bridge are color-coded with elongated (CSI < 0.4) and compacted (CSI > 0.4) morphologies, and square zones. (**c**) Statistical tree representation of the experimental probabilities for elongated and compacted states over three generation of successive crossings (N ≥ 3 replicates for each condition). (**d**) Histogram representation of the probabilities for elongated, P(E), and compacted, P(C), states for various combinations of morphological switches: elongated to elongated P(E | E), compacted to compacted P(C | C), elongated to compacted P(E | C) and compacted to elongated P(C | E). Data are presented as mean values ± SD.

https://doi.org/10.1038/s41567-025-02980-z

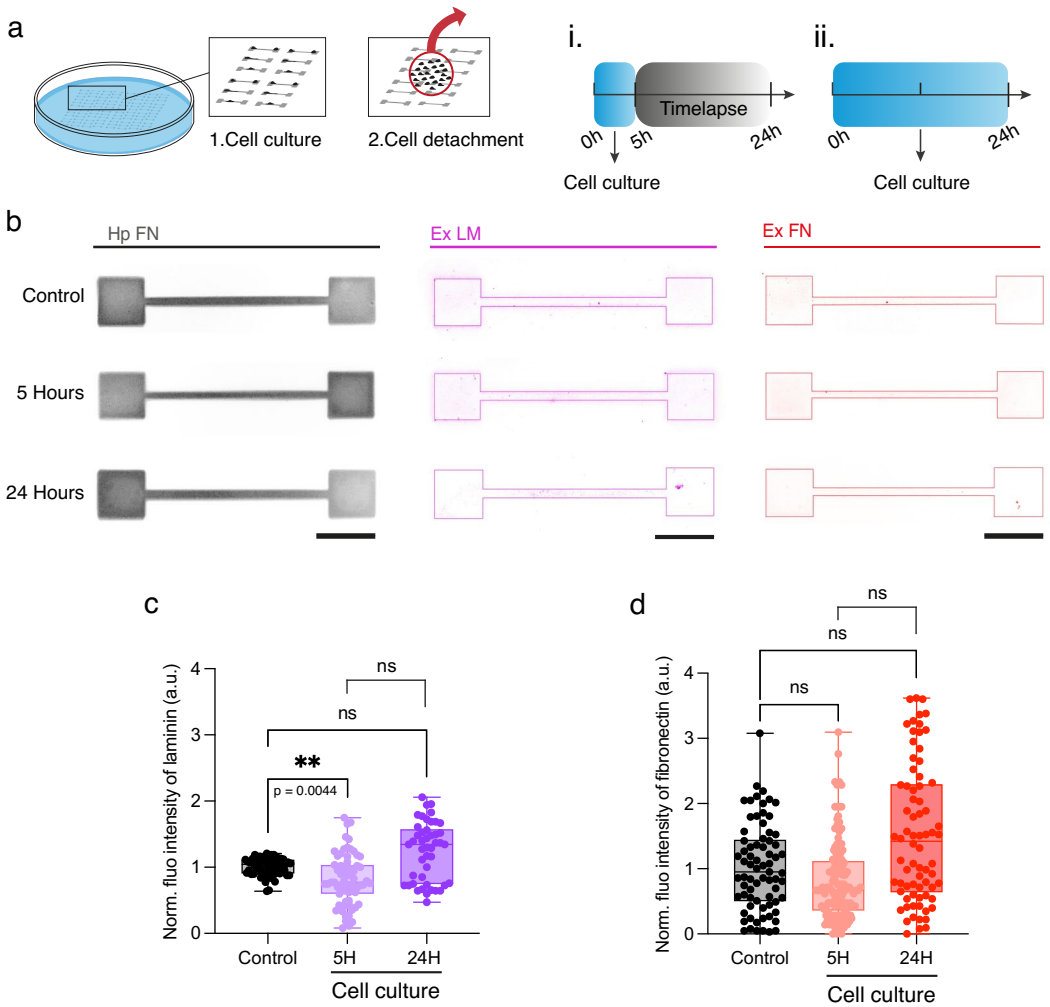

Extended Data Fig. 5 | Physico-chemical footprints. (**a**) Schematic representation of the two experimental procedures used to assess pattern conditioning by migrating cells. Cells were seeded on human plasma (hp) fibronectin (FN) micropattern, then detached and fixed either (i) after 5 hours (before the time-lapse) or (ii) 24 hours (after the time-lapse) of culture on micropatterns. (**b**) Epifluorescence images showing human plasma fibronectin, cellular laminin and cellular FN in control conditions after t = 5 h and t = 24 h of cell culture (top to bottom). Scale bar, 50 µm. (**c**) Normalized laminin intensity for control (n = 62 patterns, N = 3), 5-hour conditioning (n = 67 patterns, N = 3), and 24-hour conditioning (n = 46 patterns, N = 3). (**d**) Normalized fibronectin intensity from control (n = 73 patterns, N = 3), 5-hour conditioning (n = 125 patterns, N = 3), and 24 hour-conditioning (n = 74 patterns, N = 3). Boxplots range from the first quartile (Q1) to the third quartile (Q3), with the median (50th percentile) indicated by a line. Whiskers extend from the box to the minimum and maximum data points within 1.5 times the interquartile range.**p < 0.01, ns = not significant (Kruskal-Wallis test).

https://doi.org/10.1038/s41567-025-02980-z

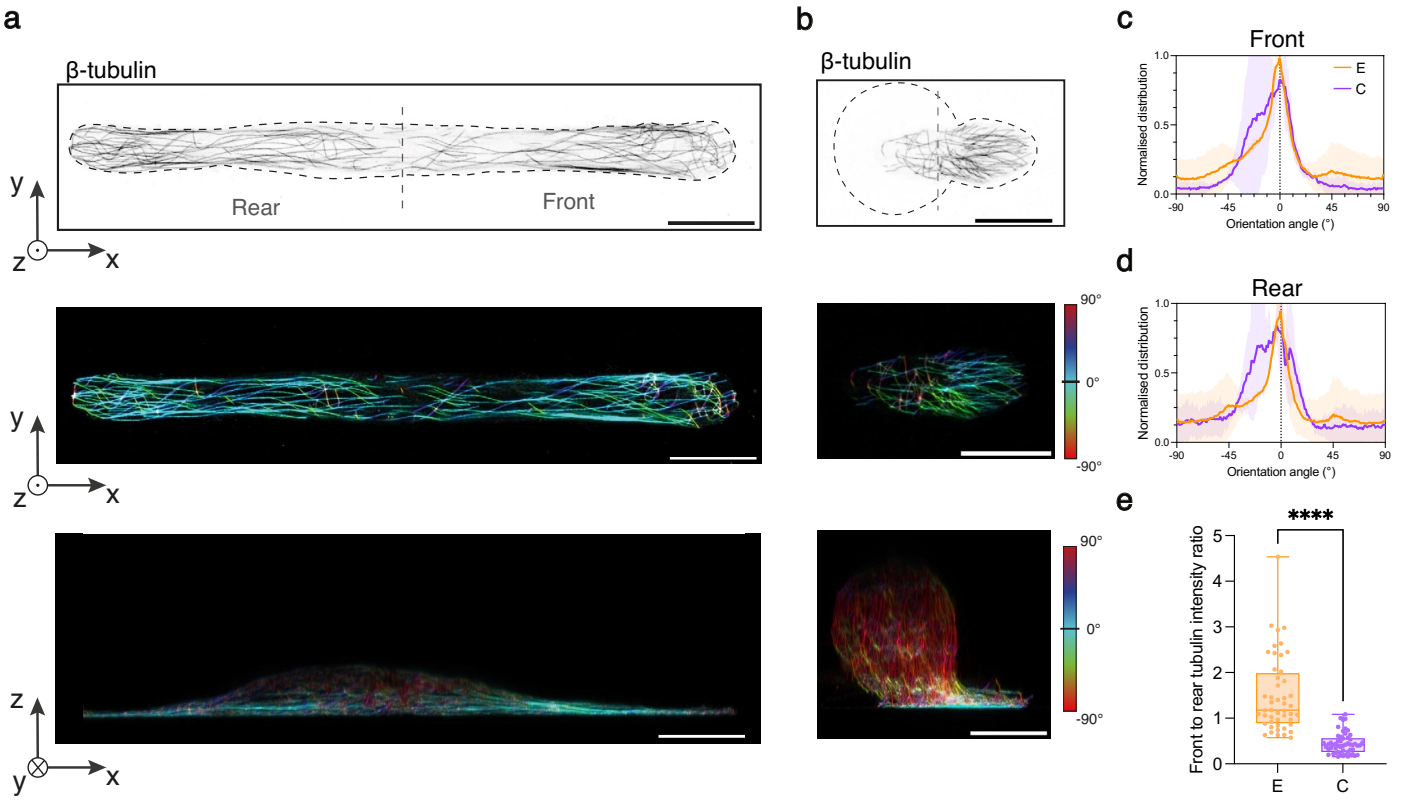

Extended Data Fig. 6 | Spatial distribution of microtubule filaments. Confocal microscopy images in enhanced-resolution mode of the basal planes of (**a**) elongated (left) and (**b**) compacted (right) cell morphologies. β-tubulin staining (inverted image) and the cell body outline is represented with a black dashed line. Scale bar, 20 µm. In bottom images, β-tubulin filaments in elongated and compacted cells were color-coded according to their spatial orientation. Scale bar, 20 µm. Distribution of the normalized intensity of microtubules (**c**) at the front and (**d**) at the rear of elongated (n = 3, N = 2) and compacted (n = 2, N = 2) cell morphologies. (**e**) Front-to-rear tubulin intensity ratio of elongated (n = 48, N = 3) and compacted (n = 54, N = 3) morphologies during crossing events. Boxplots range from the first quartile (Q1) to the third quartile (Q3), with the median (50th percentile) indicated by a line. Whiskers extend from the box to the minimum and maximum data points within 1.5 times the interquartile range. ****$p < 0.0001$ (Student's t test).

https://doi.org/10.1038/s41567-025-02980-z

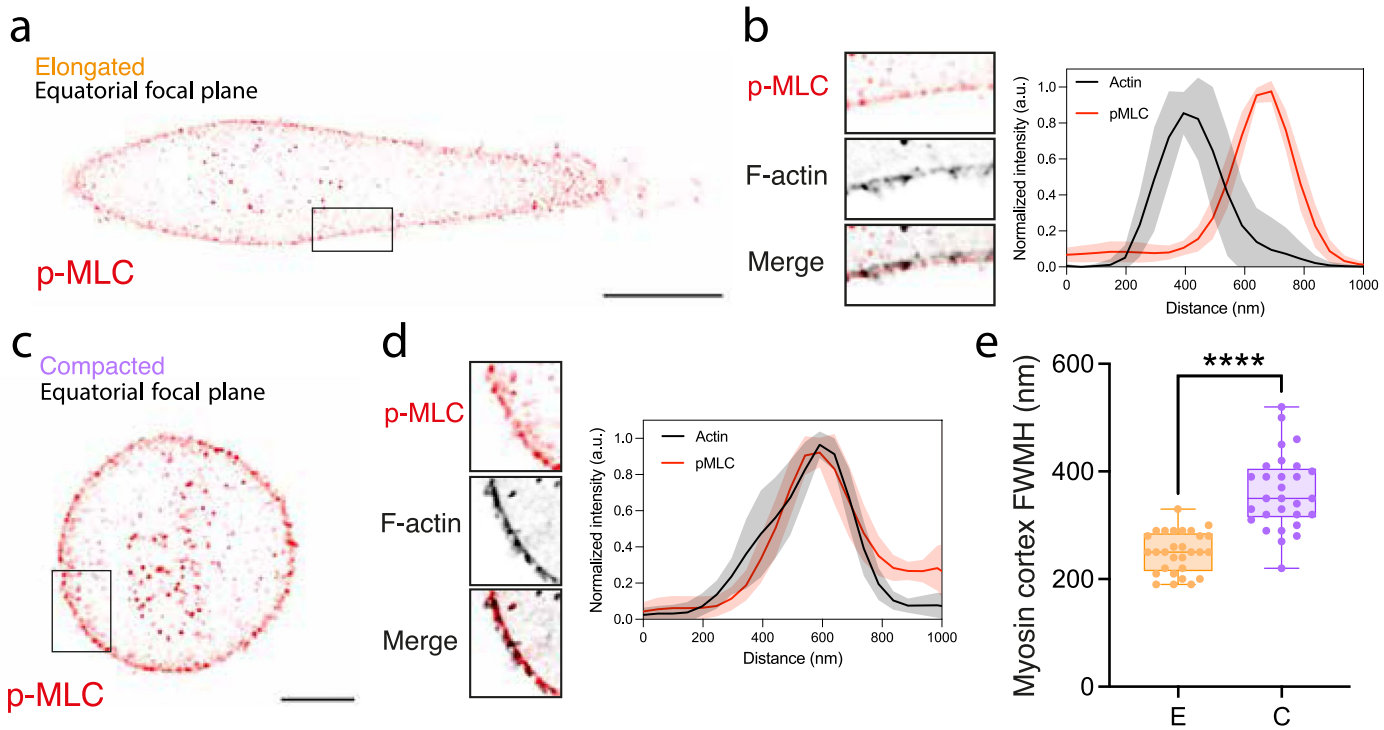

Extended Data Fig. 7 | Myosin cortex in elongated and compacted cells. Typical equatorial focal plane obtained in enhanced-resolution microscopy showing the spatial distribution of phosphorylated myosin light chain (p-MLC) at the actin cortex in (**a**-**b**) elongated and (**c**-**d**) compacted cells. Plot profiles in (**b**) and (**c**) shows the normalized intensity of actin and p-MLC as a function of the distance from the membrane. (**e**) Full width at half maximum (FWHM) for myosin cortex in elongated (orange, n = 29) and compacted (purple, n = 29) cells. Boxplots range from the first quartile (Q1) to the third quartile (Q3), with the median (50th percentile) indicated by a line. Whiskers extend from the box to the minimum and maximum data points within 1.5 times the interquartile range. ****$p < 0.0001$ (Student's t test). Scale bars, 10 µm.

https://doi.org/10.1038/s41567-025-02980-z

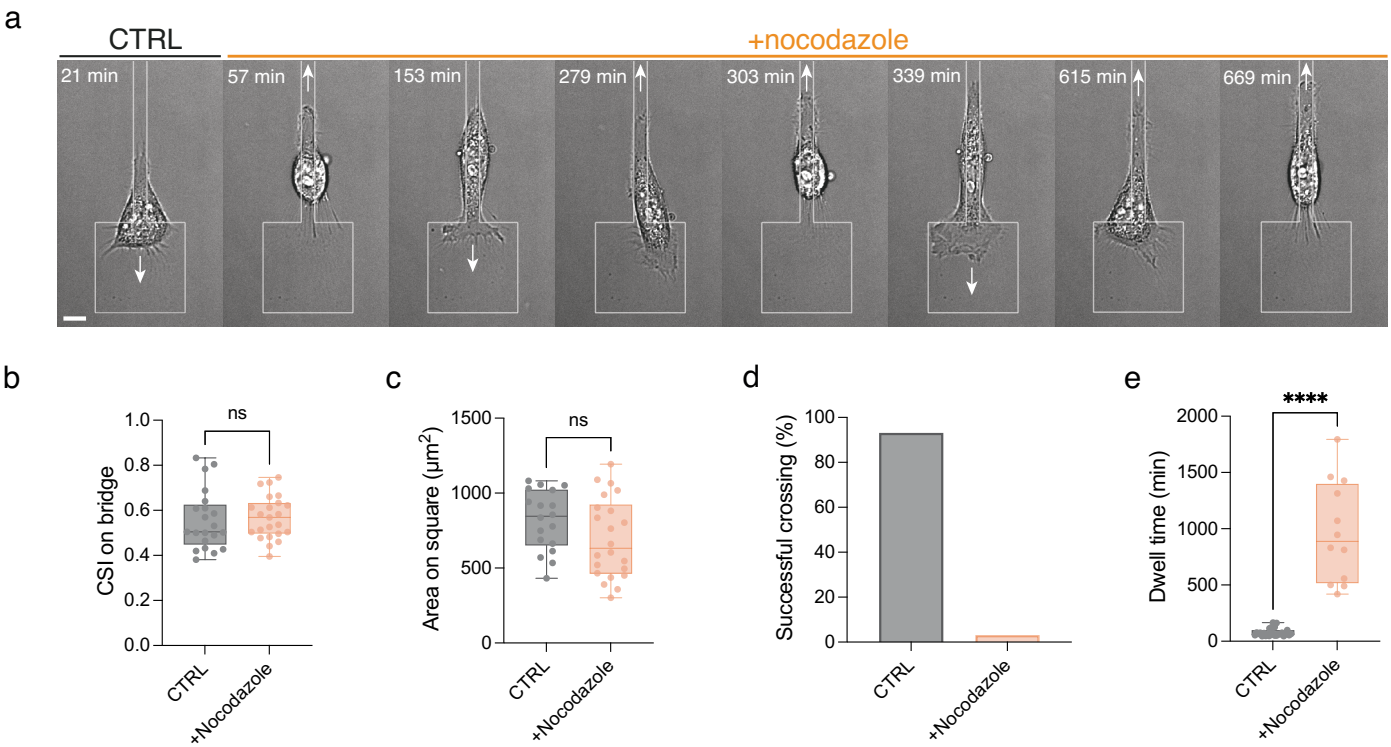

Extended Data Fig. 8 | Effect of a nocodazole treatment on confined migration. (**a**) Time-lapse sequence of a compacted cell entering a bridge before (control, CTRL) and after treatment with nocodazole (orange). CTRL is DMSO for nocodazole experiments. Scale bar, 10 µm. White arrows show the direction of migration. (**b**) Cell shape index on bridge for CTRL (n = 21, N = 5) and nocodazole-treated cells (n = 23, N = 6). (**c**) Cell area on square for CTRL (n = 18, N = 6) and nocodazole-treated cells (n = 22, N = 7). (**d**) Successful crossing percentage for CTRL (n = 146, N = 18) and nocodazole-treated cells (n = 33, N = 8) and (**e**) dwell time on square for CTRL (n = 22, grey) and nocodazole-treated cells (n = 12, light orange). Boxplots range from the first quartile (Q1) to the third quartile (Q3), with the median (50th percentile) indicated by a line. Whiskers extend from the box to the minimum and maximum data points within 1.5 times the interquartile range.****$p < 0.0001$ and n.s. = not significant (Student's t test).

https://doi.org/10.1038/s41567-025-02980-z

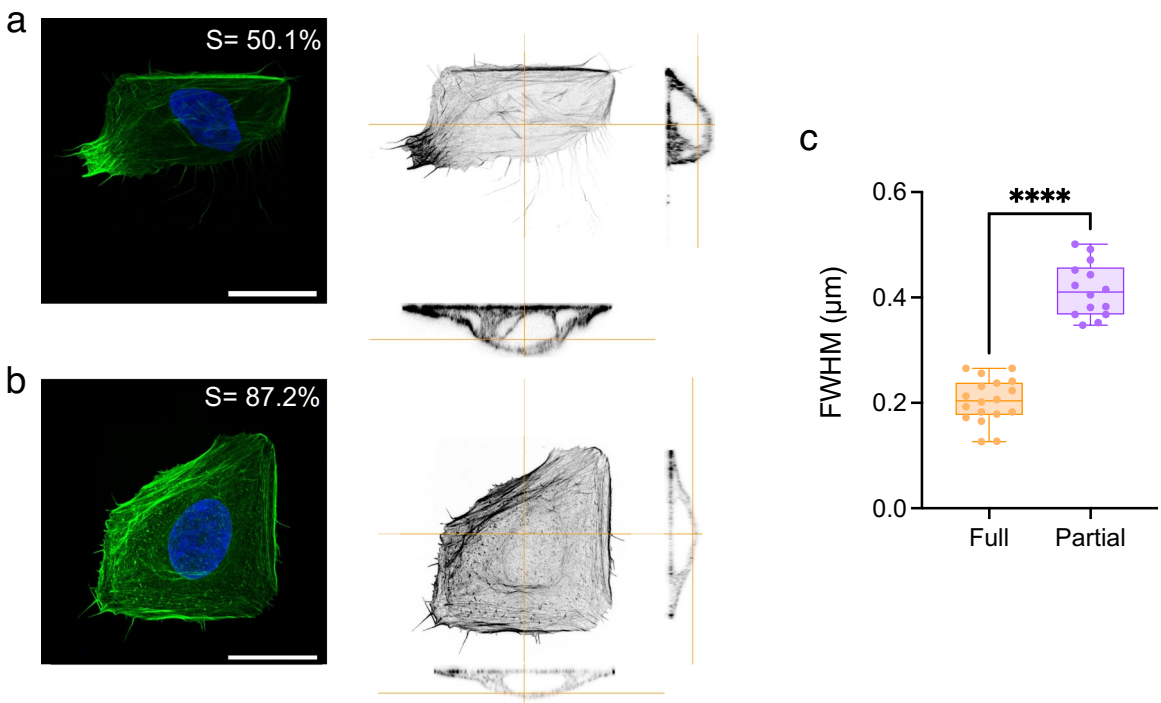

Extended Data Fig. 9 | Thickness of the actin cortex in cells spread on squares. Enhanced-resolution confocal images of (**a**) a partial spreading and (**b**) a full spreading of epithelial cells on FN square of 1600 µm^2. Cells are immunostained for F-actin with phalloidin (in green) and DNA with DAPI (in bue). Inverted images show normal and side views of the actin cytoskeleton at the apical side. The spreading rate is 50.1% for partial spreading (a) and 87.2% for full spreading (b). Scale bars, 20 µm. (**c**) Full width at half maximum (FWHM) represents the actin cortex thickness for partial (n = 14, N = 4) and full (n = 18, N = 4) spreading conditions. Boxplots range from the first quartile (Q1) to the third quartile (Q3), with the median (50th percentile) indicated by a line. Whiskers extend from the box to the minimum and maximum data points within 1.5 times the interquartile range. ****p < 0.0001 (Student's t test).

https://doi.org/10.1038/s41567-025-02980-z

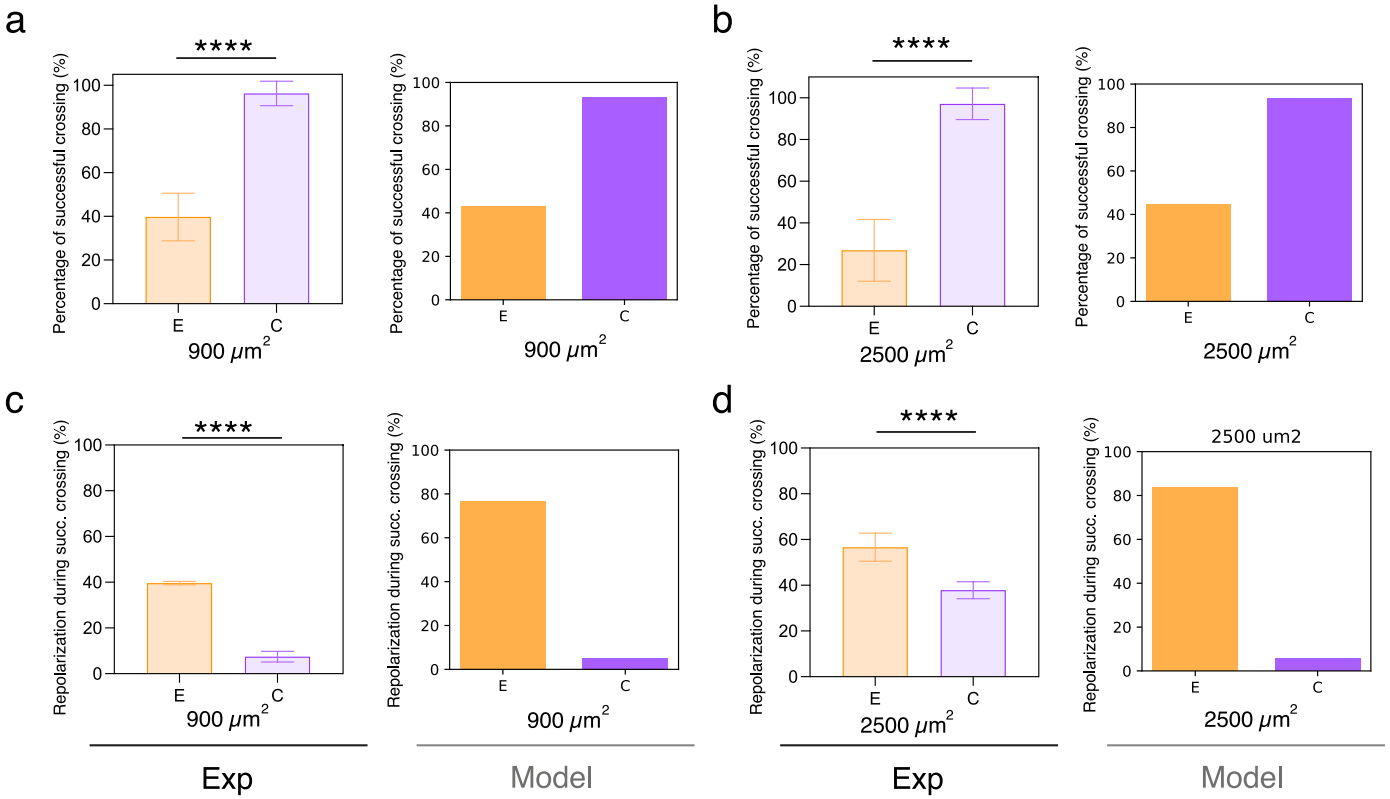

Extended Data Fig. 10 | Experimentally measured and simulated percentages of successful crossing on interconnected dumbbell micropattern. Percentages of successful crossing with (**a**) 900 μm² squares for elongated (E, n = 34, N = 3) and compacted (C, n = 34, N = 3) and (**b**) 2500 μm² squares for elongated (E, n = 50, N = 3) and compacted (C, n = 50, N = 3). Experimentally measured and model-estimated percentages of repolarization during successful crossing on interconnected dumbbell micropattern with (**c**) 900 μm² squares for elongated (E, n = 21, N = 3) and compacted (C, n = 30 cells, N = 3)cells and (**d**) 2500 μm² squares for elongated (E, n = 41, N = 3) and compacted (C, n = 27 cells, N = 3) cells. Data are presented as mean values ± SD. ****p < 0.0001 (Student's t test).

nature portfolio

Corresponding author(s): David Brückner and Sylvain Gabriele

Last updated by author(s): Jun 4, 2025

Reporting Summary

Nature Portfolio wishes to improve the reproducibility of the work that we publish. This form provides structure for consistency and transparency in reporting. For further information on Nature Portfolio policies, see our Editorial Policies and the Editorial Policy Checklist.

Statistics

For all statistical analyses, confirm that the following items are present in the figure legend, table legend, main text, or Methods section.

n/a	Confirmed	
☐	☒	The exact sample size (*n*) for each experimental group/condition, given as a discrete number and unit of measurement
☐	☒	A statement on whether measurements were taken from distinct samples or whether the same sample was measured repeatedly
☐	☒	The statistical test(s) used AND whether they are one- or two-sided *Only common tests should be described solely by name; describe more complex techniques in the Methods section.*
☒	☐	A description of all covariates tested
☐	☒	A description of any assumptions or corrections, such as tests of normality and adjustment for multiple comparisons
☐	☒	A full description of the statistical parameters including central tendency (e.g. means) or other basic estimates (e.g. regression coefficient) AND variation (e.g. standard deviation) or associated estimates of uncertainty (e.g. confidence intervals)
☐	☒	For null hypothesis testing, the test statistic (e.g. *F*, *t*, *r*) with confidence intervals, effect sizes, degrees of freedom and *P* value noted *Give P values as exact values whenever suitable.*
☒	☐	For Bayesian analysis, information on the choice of priors and Markov chain Monte Carlo settings
☒	☐	For hierarchical and complex designs, identification of the appropriate level for tests and full reporting of outcomes
☒	☐	Estimates of effect sizes (e.g. Cohen's *d*, Pearson's *r*), indicating how they were calculated

Our web collection on statistics for biologists contains articles on many of the points above.

Software and code

Policy information about availability of computer code

Data collection	Nikon A1R confocal image acquisition tool, Nikon NIS Eelements Advanced Research
Data analysis	Images and raw data were quantified with FIJI and NIS Elements Advanced Research, plotted with Graphpad Prism v10 and Matlab R2018b. Figures were organized and prepared in Illustrator CC 2024

For manuscripts utilizing custom algorithms or software that are central to the research but not yet described in published literature, software must be made available to editors and reviewers. We strongly encourage code deposition in a community repository (e.g. GitHub). See the Nature Portfolio guidelines for submitting code & software for further information.

Data

Policy information about availability of data

All manuscripts must include a data availability statement. This statement should provide the following information, where applicable:

- Accession codes, unique identifiers, or web links for publicly available datasets
- A description of any restrictions on data availability
- For clinical datasets or third party data, please ensure that the statement adheres to our policy

Provide your data availability statement here.

Research involving human participants, their data, or biological material

Policy information about studies with human participants or human data. See also policy information about sex, gender (identity/presentation), and sexual orientation and race, ethnicity and racism.

Reporting on sex and gender	NA
Reporting on race, ethnicity, or other socially relevant groupings	NA
Population characteristics	NA
Recruitment	NA
Ethics oversight	NA

Note that full information on the approval of the study protocol must also be provided in the manuscript.

Field-specific reporting

Please select the one below that is the best fit for your research. If you are not sure, read the appropriate sections before making your selection.

☒ Life sciences ☐ Behavioural & social sciences ☐ Ecological, evolutionary & environmental sciences

For a reference copy of the document with all sections, see nature.com/documents/nr-reporting-summary-flat.pdf

Life sciences study design

All studies must disclose on these points even when the disclosure is negative.

Sample size	Throughout the study, averages over multiple cells were performed and the results were successfully reproduced. Sample sizes (n) and replicates (N) are indicated at the relevant location in manuscript.
Data exclusions	No data were excluded for analysis.
Replication	All the experiments were successfully repeated with similar results.
Randomization	No specific randomization method was used, samples were processed and allocated according to specific experimental conditions and treatments.
Blinding	o blinding was used (see answer to section 4 for randomization).

Reporting for specific materials, systems and methods

We require information from authors about some types of materials, experimental systems and methods used in many studies. Here, indicate whether each material, system or method listed is relevant to your study. If you are not sure if a list item applies to your research, read the appropriate section before selecting a response.

Materials & experimental systems

n/a	Involved in the study
☐	☒ Antibodies
☐	☒ Eukaryotic cell lines
☒	☐ Palaeontology and archaeology
☒	☐ Animals and other organisms
☒	☐ Clinical data
☒	☐ Dual use research of concern
☒	☐ Plants

Methods

n/a	Involved in the study
☒	☐ ChIP-seq
☒	☐ Flow cytometry
☒	☐ MRI-based neuroimaging

Antibodies

Antibodies used	MCF-10A epithelial cells were fixed with 4% paraformaldehyde (PFA) in PBS for 15 min at room temperature after cell migration experiments. Subsequently, cells were washed three times with PBS, with the last wash lasting for 5 min, and permeabilized using 0.05% Triton X-100 in PBS for 15 min at room temperature. After another round of three washes in PBS, permeabilized cells were

	blocked with a solution of 5 v/v% Fetal Bovine Serum (FBS, Gibco) and 1 w/v % Bovine Serum Albumin (BSA, Merck) in PBS for 30 minutes at room temperature. Actin filaments were stained with AlexaFluor 488 phalloidin (Invitrogen, 1:200), the nucleus with 4′,6-diamidino-2-phenylindole (DAPI; Invitrogen, 1:200), microtubules with an anti-tubulin antibody produced in mouse (Sigma-Aldrich, 1:200).
Validation	All these antibodies has previously been used in published articles which are referred in the text.

Eukaryotic cell lines

Policy information about cell lines and Sex and Gender in Research

Cell line source(s)	MCF10A cell line was obtained from Sigma
Authentication	NA
Mycoplasma contamination	Cell lines tested negatively for the Mycoplasma contamination.
Commonly misidentified lines (See ICLAC register)	No commonly misidentified cell lines were used.

Plants

Seed stocks	NA
Novel plant genotypes	NA
Authentication	NA